Article

Not peer-reviewed version

Thermodynamic Factors Controlling Electron Transfer amongst the Terminal Electron Acceptors of Photosystem I: Insight from Kinetic Modelling

Stefano Santabarbara * and Anna Paola Casazza

Posted Date: 12 August 2024

doi: 10.20944/preprints202408.0661.v1

Keywords: electron transfer; standard gibbs free energy difference; reorganisation energy; tunnelling barrier; iron-sulphur cluster; (Phyllo)quinone

doi:10.20944/preprints202408.0661.v1

Article

Thermodynamic Factors Controlling Electron Transfer amongst the Terminal Electron Acceptors of Photosystem I: Insight from Kinetic Modelling

Stefano Santabarbara * and Anna Paola Casazza

Photosynthesis Research Unit, Consiglio Nazionale delle Ricerche, Via A. Corti 12, 20133 Milano, Italy
* Correspondence: stefano.santabarbara@cnr.it

Abstract: Photosystem I is a key component of primary energy conversion in oxygenic photosynthesis. Electron transfer reactions in Photosystem I take place across two, parallel, electron transfer chains that converge after a few electron transfer steps, sharing both the terminal electron acceptors, that are a series of three Iron-Sulphur (Fe-S) clusters known as F_X, F_A and F_B, and the terminal donor, P_{700}. The two electron transfer chains show kinetic differences which are, due to their close geometrical symmetry, mainly attributable to the tuning of the physical-chemical reactivity of the bound cofactors, exerted by the protein surroundings. The factors controlling the rate of electron transfer between the terminal Fe-S clusters are still not fully understood because of the difficulties of monitoring these events directly. Here we present a discussion concerning the driving forces associated to electron transfer between F_X and F_A as well as F_A and F_B, employing a tunnelling-based description of the reaction rates coupled to the kinetic modelling of forward and recombination reactions. It is concluded that the reorganisation energy for F_X^- oxidation shall be lower than 1 eV. Moreover, it is suggested that the analysis of mutants with altered F_A redox properties can also provide useful information concerning the upstream, phylloquinone, cofactor energetics.

Keywords: electron transfer; standard gibbs free energy difference; reorganisation energy; tunnelling barrier; iron-sulphur cluster; (Phyllo)quinone

---

1. Introduction

Photosystem I (PSI) is a fundamental component of the oxygenic photosynthetic electron transport chain. It catalyses the light-dependent oxidation of soluble electron shuttles, most commonly either the cupper-binding protein plastocyanin or the small cytochrome c_6, at its so-called donor side and the reduction of ferredoxin, which is also a soluble protein, at its acceptor side. Photosystem I is a very large membrane-embedded cofactor-protein supercomplex, composed of more than 10 protein subunits (e.g. [1,2]), the exact number of which depends on the species. Under an operational perspective it can be considered as being composed, analogously to the other photosystems, of two functional moieties: i) a core complex which has the role of harvesting sunlight and to perform primary charge separation and successive charge stabilisation through electron transfer (ET) reactions involving a series of redox-active cofactors, and ii) a peripheral antenna, which has light harvesting function only, and which composition in terms of proteins and chromophores, varies largely amongst different organisms.

The characteristics of the subunits composing the core complex of PSI appear instead to be generally well-conserved throughout evolutionary divergent species, particularly considering the two largest subunits PsaA and PsaB which form an heterodimer and coordinate, together with the core-antenna pigments, the majority of the redox-active cofactors. Also well conserved is the PsaC subunit which binds two 4Fe-4S clusters, referred to as F_A and F_B, acting as the terminal electron acceptors within the photosystem and being, in turn, responsible for ferredoxin reduction. Structural studies [3–5] have shown that, in analogy to all other known photosynthetic reaction centres, the PsaA- and PsaB-coordinated cofactors, identified as participating in ET reactions, are organised in a highly symmetric fashion. The redox-active cofactors display a mirror symmetry arrangement with

Preprints.org (www.preprints.org) | NOT PEER-REVIEWED | Posted: 12 August 2024 doi:10.20944/preprints202408.0661.v1

respect to the reference axis being putatively perpendicular to the membrane plane (Figure 1A). The symmetric organisation of the cofactors results in the presence of two putative ET chains, which are however not completely independent, sharing the (hetero)dimer of Chlorophyll (Chl) *a*/Chl *a*′ (the latter being an epimer [3]), assigned to the long-lived, terminal, electron donor, $P_{700}^{(+)}$ and the 4Fe-4S cluster F_{X}, which is the last PsaA/PsaB-bound acceptor before the PsaC-bound F_{A} and F_{B} centres. Both P_{700}, where the number indicates the maximal absorption bleaching upon oxidation [2,6], and F_{X} are coordinated at the interface of PsaA and PsaB.

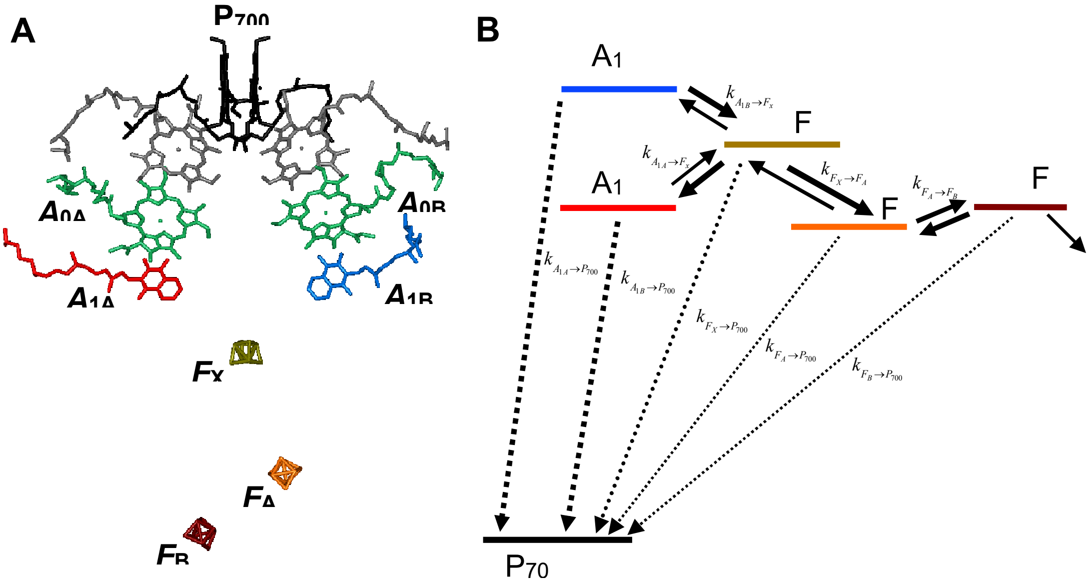

Figure 1. Panel A: Arrangement of the redox active cofactors in PS I (from the structural model of Jordan et al. (2001) PDB file # 1JB0). The terminal electron donor ($P_{700}^{(+)}$) is considered as Chl *a*/Chl *a*′ hetero-dimer, is shown in black; the so-called accessory Chl *a* are unlabeled and are shown in grey; the primary Chl *a* electron acceptors $A_{0\mathrm{A,B}}^{(-)}$ are shown in green; the phylloquinone $A_{1\mathrm{A}}^{(-)}$ is own in red and $A_{1\mathrm{B}}^{(-)}$ in blue. The terminal 4Fe-4S clusters, F_{X}, F_{A} and F_{B} are shown in gold, orange and burgundy colour, respectively. **Panel B:** Kinetic scheme utilised in the simulations of electron transfer reactions. Solid arrow indicates forward and backwards rates between pairs of successive redox-active cofactors. Dash and dotted lines represent charge recombination reactions between individual cofactors and P_{700}^{+}, involving the phylloquinones and iron-sulphur clusters, respectively. The colour code is the same as in (**A**) and is maintained throughout the manuscript. Note that the energy gaps are not scaled. Properly scaled E^{0} are shown in Figures 2 and 3.

A general consensus has been reached over the years that in PSI the two parallel cofactor chains are both functional ([2,7–12]) and references therein). This represents a major functional difference with respect to Photosystem II, and the purple bacteria Reaction Centre (RC), in which primary photochemistry and ET reactions involve exclusively one cofactor chain, with the exclusion of the terminal electron acceptor, the quinone Q_{B}, which is structurally part of the “inactive” chain, but accepts electrons from the “photochemically functional chain” bound quinone, Q_{A}, instead. The need to control inter-quinone ET and the full-reduction of Q_{B} to quinole, by two consecutive charge separation events, is thought to be one of the main reasons for having an asymmetric, also referred to as mono-directional, ET in Type II photosynthetic RC. In PSI, and generally in Type I RC to whom it belongs, ET reactions involve only one-electron exchange, so that the need to control the accumulation of either oxidative or reducing equivalent at any level of the ET chain is not stringent.

Nonetheless, the probability by which electrons are transferred by each ET chain of PSI remains somewhat debated, with figures ranging from almost equal utilisation [12–19], to very asymmetric proportions in favour of the PsaA-coordinated branch [20–24]. Further functional differences are also apparent at the level of intermediate steps, particularly in the lifetime of oxidation of the reduced phylloquinone, A_1 , by next acceptor in the chain, F_X . This reaction shows a complex kinetic behaviour, which in its simplest description is accounted by two main phases characterised by lifetimes of 5-20 ns and 200-300 ns [6–10,25,26]. Studies of mutants at the level of the phylloquinone binding site have led to the assignment of the 200-300 ns phase to the oxidation of $A_{1\mathrm{A}}^-$ [6–10,27–31] (the subscript indicates the subunit which primarily coordinates the cofactor) and the 5-20 ns phase to the oxidation of $A_{1\mathrm{B}}^-$ [6–10,27,31]. These phases also show significantly different temperature dependences, with the slowest one displaying a larger activation energy (65-130 meV) with respect to the fast one (6-20 meV) [32–34]. Since F_X is a common cofactor to both reactions, and because of the similarity in the co-ordination geometry of the phylloquinones, the one-order-of-magnitude difference in the $A_{1\mathrm{A}}^-$ and $A_{1\mathrm{B}}^-$ oxidation kinetics was attributed, in the framework of ET-theory (e.g. [35–37] and references therein), to an asymmetry in the driving force for these reactions, with $A_{1\mathrm{B}}^-$ oxidation being more thermodynamically favourable (*e.g.* $\Delta G^0_{A_{1\mathrm{B}}\to F_\mathrm{X}} < \Delta G^0_{A_{1\mathrm{A}}\to F_\mathrm{X}}$) [7,11,38,39]. Even though there is a general consensus concerning this interpretation, different estimates for the free energies have been advanced, also depending on the approach utilised for their evaluation ([12] and reference therein). Because of the very negative value of the phylloquinone potential direct redox titration is, at least, cumbersome [40]. Contradictory results were also obtained for the titration of F_X , although its potential ($E^0_{F_\mathrm{X}}$) can be safely regarded as less than –680 mV ([41–43] and see discussion in [**6**]). Moreover, even direct titration can suffer of the bias linked to progressive accumulation of charges on the acceptor side (*i.e.* on F_A , F_B , F_X and so on). The direct electrochemically determined midpoint potentials can therefore differ, also significantly, from the "operational" ones, when the nearby cofactors are oxidised instead (see Ptsushenko *et al.* [44] for further discussion). Thus, most of the estimated $A_{1\mathrm{A}}$ and $A_{1\mathrm{B}}$ redox potentials were derived either from ET-theory-based modelling of the oxidation kinetic [7,11,38,39] or from structure-based computational methods [44–47]. None of these approaches is fully water-proof, since both require some specific simplifications and assumptions to address the problem. A detailed description of these issues is beyond the scope of the present paper. Yet, currently only two energetic pictures were proven to account for the oxidation kinetics at room temperature, the temperature dependence of the reactions [48] and the effect of mutations in the phylloquinone binding site, at least, in the latter case, concerning the $A_{1\mathrm{A}}^-$ to F_X reaction [49], for which information are more abundant. These are the so-called "weak driving force" and "large driving force" scenarios. In the former, $A_{1\mathrm{A}}^-$ oxidation is associated with a free energy difference of ~ -30 meV $< \Delta G^0_{A_{1\mathrm{A}}\to F_\mathrm{X}} < +30$ meV whereas $A_{1\mathrm{B}}^-$ oxidation with $\Delta G^0_{A_{1\mathrm{B}}\to F_\mathrm{X}} < -50$ meV (note that the values are broad, and rounded, because they depend on the exact parameters set describing the reaction rate constants) [7,11,12,48,49]. It is worth noticing that in the lower driving force limit $A_{1\mathrm{A}}^-$ oxidation becomes thermodynamically unfavourable. Within the weak-driving force configuration, experimental observable are semi-quantitatively reproduced considering a total reorganisation energy (λ_{tot}) associated to phylloquinone oxidation, as well as F_A reduction by F_X , of about 0.7 eV [7,11,12,48,49]. The "large driving force" scenario invokes that both $\Delta G^0_{A_{1\mathrm{A}}\to F_\mathrm{X}}$ and $\Delta G^0_{A_{1\mathrm{B}}\to F_\mathrm{X}}$ $< -$ 50/75 meV and that $\Delta G^0_{A_{1\mathrm{B}}\to F_\mathrm{X}} \ll \Delta G^0_{A_{1\mathrm{A}}\to F_\mathrm{X}}$, with the former corresponding to driving forces even larger than ~150 meV [39,44]. This energetic configuration, however, required to consider much larger reorganisation energies, in the order of 1 eV [48,49], to describe the experimental phylloquinone oxidation kinetics. When assuming an homogenous value of λ_{tot} for all the ET reactions, the difference in the values adopted to simulate A_1^- oxidation (*i.e.* 1 eV with respect to 0.7 eV) resulted in pronounced differences in the simulations of F_X oxidation for the two energetic configurations described above even when keeping all other relevant simulation parameters, including $\Delta G^0_{F_\mathrm{X}\to F_\mathrm{A}}$ which was set at ~ –150 meV [6,7], equal. In this framework, the electron transfer from F_X to the terminal Fe-S clusters was predicted to be about 5 folds slower for the large A_1^- oxidation driving force than for the weak A_1^- oxidation driving force enegetics ([48] and vide infra for further detail).

The redox potential of the iron-sulphur clusters F_A an F_B is, together with the one of P_{700}^+, the more accurately determined, even in place of some variability in the estimations [6,50–53]. Knowledge of these values shall increase the margin of accuracy of kinetic modelling predictions. Nonetheless, the dynamics of ET involving these redox centres are not unambiguously understood yet. This is mainly due to the optical properties of the Fe-S cluster, which possess a broad, relatively unstructured spectrum that abundantly overlaps with those of other PSI-bound chromophores [54,55]. Moreover, ET involving species having close-to-the-same absorption spectra imply a small differential extinction coefficient, making their direct detection by optical methods extremely challenging. Most of the kinetic information relies then on alternative methods, exploiting changes in the electric field through the protein milieu caused by the electron displacement along the ET chain. These include direct methods, such as photovoltage [56–60], and indirect optical probes, like ET-dependent local-stark effect on chlorophylls and carotenoids [25]. From these methods a relatively broad range of values for the F_X to F_A / F_B transfer time have been proposed, ranging from less than 25 ns to ~300 ns ([26,61] and references therein). A kinetic phase characterised by lifetimes of 160-180 ns, and attributed to ET between the iron-sulphur clusters, was also resolved in mutants in which the A_{1A}^- oxidation phase, to which it is otherwise overlapped, was slowed-down more than 3 times [30,62,63]. A component with similar lifetime is also resolvable in wild-type photosystems in temperature dependence studies, when it appears to have a lower activation, and becomes therefore discernible from the slow phase of $A_{1(A)}^-$ oxidation upon cooling [33,34]. Electron transfer between F_A and F_B is even less characterised, as the positioning of these cofactors leads to a vectorial ET almost parallel to the membrane plane (perpendicular to the symmetry axis) which is unfavourable for both local-stark and photo-voltage detection. Hence, either only the collective transfer to F_A / F_B is generally detected or, alternatively, transfer to F_A alone after F_B is chemically inactivated/destabilised [26,61]. It is commonly assumed that the transfer time across all of the Fe-S shall be faster than 500 ns – 1 μs to account for the rapid reduction of pre-bound ferredoxin, that takes place in about 1 to 3 μs, although even faster sub-microsecond kinetics have been reported [64].

In order to gain further insight into the dynamics of ET reactions involving the Fe-S of PSI, kinetic simulations are here presented in which the effect of the most crucial thermodynamic parameters, *i.e.* the standard free energy difference and the reorganisation energy, are explored. The ET reactions involving the Fe-S clusters are contextualised within the “weak” and “large” driving force energetic scenarios for A_1^- oxidation. The simulations allow to put forward predictions which could be, in principle, tested experimentally to get a better understanding of these ET events.

2. Results and Discussion

In order to gain some additional information concerning the ET reactions involving the 4Fe-4S centres in PSI, *i.e.* the reduction of F_A by F_X^- (hereafter the sign indicates the reduced state of the FeS centre, not its net charge) and the successive reduction of F_B by F_A^-, kinetics simulations were performed starting from the two energetic scenarios which provide a satisfactory, semi-quantitative, description for the wild-type PSI. Successively, perturbations of parameters that control the rate constants of ET between the FeS clusters, mainly the standard free energies (ΔG_{DA}^0) and the reorganisation energy (λ_{tot}), are introduced.

2.1 Weak Driving Force Scenario for A_1^- Oxidation

Figure 2 shows the simulated population evolutions of the reduced ET cofactors in PSI, after initial population of phylloquinones A_{1A} and A_{1B}, within the so-called “weak-driving” force framework. The parameters used in the calculations are reported in Table 1. In brief, the standard free energy difference for A_{1A}^- and A_{1B}^- oxidation were taken as $\Delta G_{A_{1A} \to F_X}^0$ = +10 meV and

$\Delta G^0_{A_{1B}\rightarrow F_X}$ = –50 meV, and those for the 4Fe-4S centres oxidation were $\Delta G^0_{F_X\rightarrow F_A}$ = –150 meV and $\Delta G^0_{F_A\rightarrow F_B}$ = +25 meV. The two latter fall within the range derivable from direct redox titrations of the FeS cofactors [50–53]. Setting the midpoint potential of F_B at –555 mV, it then results that $E^0_{F_A}$ = –530 mV, $E^0_{F_X}$ = –680 mV $E^0_{A_{1A}}$ = –670 mV and $E^0_{A_{1B}}$ = –730 mV. Because of the relative spread of experimentally retrieved E^0 values and considering the effect of piling-up reducing equivalents upon titrations which likely result in a bias in the determined FeS clusters redox potentials, the free energy differences calculated from the experimental titrations and those employed in the simulations might and shall not match exactly. Those used in the simulations rather reflect the so-called "operational" potentials. Even with these approximations, the general consideration that the energy gap between F_X and F_A is relatively large, whereas the one between F_A and F_B is shallow, with the two PsaC-coordinated centres being almost iso-potential, remains valid. For the parameters described above, and in general for the "weak driving" force model, it is possible to consider a common value of the reorganisation energy for the A^-_{1A}, A^-_{1B} and F^-_X oxidation equal to 0.7 eV whereas a larger value of 0.9 eV was considered for F^-_A oxidation. This is justified since the outer shell reconfiguration is expected to be larger for reactions involving metal centres only with respect to organic cofactors.

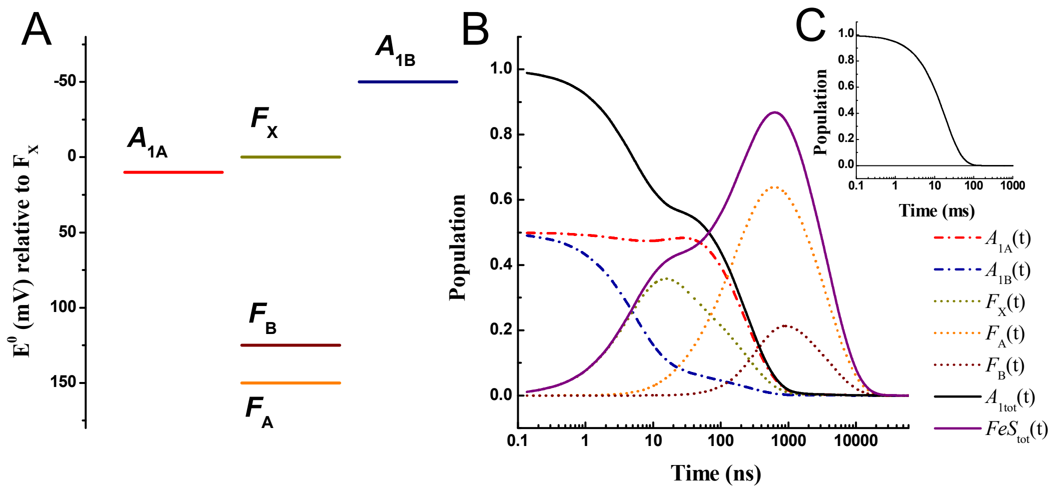

Figure 2. Panel A: reference energetic scheme for the "weak driving force" scenario for A^-_1 oxidation; standard redox potentials (E^0) are shown relative to F_X. **Panel B:** simulated population evolution of the individual redox active cofactors, $A^-_{1A}(t)$: dashed-dot red line, $A^-_{1B}(t)$ dashed-dot blue line, $F^-_X(t)$ dot golden line, $F^-_A(t)$ dot orange line, $F^-_B(t)$ dot burgundy line. Also shown are the total population evolutions of $A^-_{1,tot}(t) = A^-_{1A}(t) + A^-_{1B}(t)$ (black line) and $FeS^-_{tot}(t) = F^-_X(t) + F^-_A(t) + F^-_B(t)$ (purple line). The inset (**C**) shows the recombination kinetics simulated in absence of an exit from the system (k_{out} = 0). Temperature: 290 K.

Specific frequencies of the mean coupled nuclear modes were considered for A^-_1 oxidation, corresponding to $\hbar\overline{\omega}_{A_{1A}\rightarrow F_X}$ = 22 meV (175 cm^{-1}) and $\hbar\overline{\omega}_{A_{1B}\rightarrow F_X}$ = 46 meV (375 cm^{-1}). These values were obtained from the analysis of the phylloquinone oxidation kinetics as a function of the temperature [66] and resulted in an improvement of the simulations of the temperature dependence of the kinetics when explicitly considered. A coupling $\hbar\overline{\omega}_{DA}$ = 34 meV (275 cm^{-1}), which is the mean of the values employed for the quinone oxidation, was used for all other reactions. In the kinetic scheme shown above (Figure 1B) also the recombination reactions between all reduced cofactors and P^+_{700} were included. In the simulations of the recombination reactions $E^0_{P_{700}}$ was +450 mV, in accordance with direct estimations from redox titrations [**6**], and the reorganisation energy was 0.9 eV for all reactions. The recombination reactions have virtually no influence on the simulations of forward ET kinetics because these rates are several order of magnitude slower than productive reactions, due to large distances between the cofactor pairs even in place of large favourable driving forces for all of these processes (see Appendix S1 of the Supplementary Information). However, their inclusion allows to compare the simulated and experimentally determined recombination kinetics, as shown in Figure 2C, simply by suppressing the exit rate from the system (*i.e.* F_{B}^{-} oxidation by external electron acceptors).

For the parameters discussed above it is obtained that, at room temperature (290 K), the system is characterised by five lifetimes (the number corresponding to the states present in the kinetics scheme) of 5.2, 22.5, 136, 243 and 3808 ns, which are common to the description of the population evolution of all cofactors. The 5.2, 22.5 and 243 ns lifetimes are those also retrieved from a three states model that does not explicitly include F_{A} and F_{B} (*e.g.* [7,11,12,48,49] and see Appendix S1 Figure S1 and Table S1), so that the remaining lifetimes of 136 and 3808 ns can be related to electron transfer reactions involving the terminal iron-sulphur cluster directly. The longest-lived lifetime describes the exit from the system, when this is considered ($F_{\mathrm{B}} \rightarrow Out$). This reaction is not modelled according to ET theory, a phenomenological rate of 1 x 10^{-3} ns^{-1} is considered instead and it is set to zero, when necessary, to simulate the recombination reactions.

Table 1. Rate-defining Parameters and Simulated ET kinetic for the weak driving force energetic scenario.

Rate Determining Parameters						Electron Transfer Simulated Parameters							
							Amplitudes						
Reaction	X_{DA} (Å)	ΔG_{DA}^{0} (eV)	$\lambda_{t,DA}$ (eV)	$\overline{\omega}_{DA}$ (eV/ cm^{-1})	$k_{D\rightarrow A}$ (ns^{-1})	τ (ns)	$p_{A_{1\mathrm{A}}}$	$p_{A_{1\mathrm{B}}}$	$p_{F_{\mathrm{X}}}$	$p_{F_{\mathrm{A}}}$	$p_{F_{\mathrm{B}}}$	$p_{A_{1\mathrm{tot}}}$	$p_{FeS_{\mathrm{tot}}}$
$A_{1A}^{-} \rightarrow F_{X}$	9.1	0.01	0.700	0.022 (175)	0.0181	5.26	0.0754	0.382	-0.489	0.033	0.000	0.457	-0.457
$A_{1B}^{-} \rightarrow F_{X}$	9.0	-0.05	0.700	0.046 (375)	0.145	22.5	-0.173	0.051	0.172	-0.051	0.003	-0.123	0.123
$F_{X}^{-} \rightarrow F_{A}$	11.6	-0.15	0.700	0.034 (275)	0.0126	136	0.0035	0.000	0.001	-0.295	0.336	0.004	0.042
$F_{A}^{-} \rightarrow F_{B}$	9.5	0.025	0.900	0.034 (275)	0.0019	243	0.587	0.067	0.312	-0.489	-0.628	0.654	-0.806
$F_{B}^{-} \rightarrow$	–	–	–	–	0.00100	3808	0.0068	0.001	0.005	0.803	0.290	0.008	1.098

Summary of the parameters utilised for the simulation of forward electron transfer in reference PSI within the weak-driving force scenario for A_{1}^{-} oxidation. The rate-defining parameters which are common to all forward electron reactions are the electronic coupling matrix element, $|H_0|^2$=1.3 10^{-3} eV^2, the barrier camping factor β=1.34 Å^{-1} and the temperature *T*=290 K, which are defined in Equation 1 of the main text.

The table also lista the lifetimes (τ_i) and associated amplitudes (p_i) describing the population evolution of each of the cofactors described in the model. The total amplitude associated with the electron transfer kinetics of phylloquinones ($p_{A_{1\mathrm{tot}}}$) and iron-sulphur centres ($p_{FeS_{\mathrm{tot}}}$) are also

doi:10.20944/preprints202408.0661.v1

presented in the table. The initial conditions for the amplitude simulations were $A_{1A}^{-}(0) = A_{1B}^{-}(0) = 0.5$ and zero on all other cofactors considered.

Within this energetic scheme, the oxidation of A_{1B}^{-} is dominated by the two fastest components (~5 and 22.5 ns), resulting in an average decay lifetime of 46 ns, whereas the oxidation of A_{1A}^{-} is dominated by the 243 ns component, and the resulting average decay is 331 ns. Despite the assumption of equal initial population at time zero of A_{1A}^{-} and A_{1B}^{-} the predicted ratio of fast (5 ns and 22.5 ns) *to* slow (all remaining ones) oxidation phases is 0.33:0.67, which was interpreted as a transient inter-quinone population transfer [67]. Since the detail of the model predictions concerning the phylloquinone ET reactions has already been discussed previously (*e.g.* [7,11,12,48,49]), more attention will be here dedicated to the transfer involving the 4Fe-4S clusters. Within the above mentioned kinetic/energetic scheme, the average reduction time of F_X is predicted to be relatively fast, and described uniquely by the 5.2 ns component, whereas the successive oxidation is multiphasic, dominated by the 22.5 and 243 ns lifetimes, giving rise to an average decay lifetime (τ_{av}) of 199 ns, which is only slightly slower than the value simulated for the total quinone oxidation ($A_{1,tot}^{-} = A_{1A}^{-} + A_{1B}^{-}$) being 160 ns. Similarly close values are obtained when comparing the mean population lifetime (*i.e.* the first moment of the population temporal evolution, τ_m), that is estimated as being 900 ns for F_X^{-} with respect to 805 ns for $A_{1,tot}^{-}$ oxidations. The τ_m are larger than the τ_{av} values because of the increased weight of the slowest component in the parameter estimation, which is at least one order of magnitude slower than all other lifetimes. When the latter is omitted from the calculations, the mean lifetimes for F_X^{-} and $A_{1,tot}^{-}$ become 240 and 243 ns, respectively, that are then close to τ_{av}. Yet, irrespectively of the parameters considered, these cofactors relax to their neutral state almost simultaneously. This would explain the difficulties in detecting an electrogenic phase specifically associated with the F_X oxidation/reduction reactions, since this would broadly overlap kinetically with A_1^{-} oxidation. The successive redox acceptors F_A and F_B are reduced with average lifetimes of 192 and 243 ns, respectively, that is, almost co-ordinately with the relaxation of $A_{1,tot}^{-}$ and F_X^{-}, and are oxidised with average lifetimes of 3.6 µs and 1.9 µs, respectively, clearly limited by the rate of exit from the system. The simulated mean lifetimes of F_A^{-} and F_B^{-} population evolutions are 4.0 µs and 4.2 µs, respectively, again indicating that the terminal acceptors are oxidised almost simultaneously, which is due to the weak, slightly endergonic, driving force associated to F_A^{-} oxidation, leading to the partitioning of reducing equivalents in favour of this cofactor, with respect to the terminal acceptor F_B.

Figure 2C also shows the predicted recombination, in the absence of an exit from the system, where the oxidation of the terminal 4Fe-S cluster is dominated by a lifetime of 19 ms, which replaces the longest-lived ~4 µs lifetime predicted from the simulations in the presence of an acceptor. The simulated recombination lifetime falls well within the spread of values reported in the literature, that most commonly are in the range of 10 – 200 ms (see [6,26,68–71] and reference therein). It is also worth mentioning that the observed lifetime, however, does not reflect the (inverse) direct recombination rate from the terminal 4Fe-4S clusters, that are simulated as 2.1 x 10^{-17} ns^{-1} and 4.8 x 10^{-22} ns^{-1} for the reactions involving F_A^{-} and F_B^{-} respectively. Rather the recombination rate/lifetime is determined by the energetically up-hill repopulation of the upstream cofactors, chiefly F_X^{-}. The predicted recombination kinetics are virtually unaffected, in the energetic framework discussed above, by arbitrarily setting to zero the values of all the recombination to P_{700}^{+}, excluding the direct recombination from the phylloquinones (Appendix S1 Figure S2).

2.2. Large Driving Force Scenario for A_1^{-} Oxidation

Figure 3 shows the simulations obtained within the "large driving force" scenario for A_1^- oxidation. In this case, we considered values of $\Delta G^0_{A_{1A}\rightarrow F_X}$ = –50 meV and $\Delta G^0_{A_{1B}\rightarrow F_X}$ = –220 meV as suggested by Milanovsky et al. [39], whereas the free energies for the other reactions were the same as discussed above, $\Delta G^0_{F_X\rightarrow F_A}$ = –150 meV and $\Delta G^0_{F_A\rightarrow F_B}$ = +25 meV. Setting the midpoint potential of F_B at –555 mV, it then results that $E^0_{F_A}$ = –530 mV, $E^0_{F_X}$ = –680 mV $E^0_{A_{1A}}$ = –730 mV and $E^0_{A_{1B}}$ = –900 mV. The parameters set employed in the calculations is listed in Table 2. In order to facilitate the comparison between the two energetic scenarios considered, whenever feasible, the same parameters were adopted in the simulations. The main difference resides in the reorganisation energy value, because within the large driving force scheme, a value of λ_{tot} = 0.7 eV associated to the quinone reactions resulted in simulated lifetimes which are too fast with respect to the measured ones, particularly for the slowest phase of A_1^- oxidation which would be simulated by a lifetime of ~100 ns, that is at least two times faster than the value retrieved from the experiments, i.e. ~250-360 ns (see Appendix S3 of the Supplementary Information Figure S4). It was therefore necessary, as also discussed previously [48], to use a larger value for λ_{tot} of 1 eV for these ET steps, that was extended to the simulation of all other, forward and recombination, reactions. Within this energetic/kinetic scenario, the simulated lifetimes, common to all reactions are: 8.2, 295, 307, 1411 and 4415 ns. The 8.2, 307 and 1411 ns lifetimes are also retrieved for a kinetic scheme that not explicitly considers the terminal iron-sulphur centres (Appendix S1 Figure S1 and Table S1), therefore the remaining 295 and 4415 ns are associated mainly to ET processes directly involving F_A and F_B.

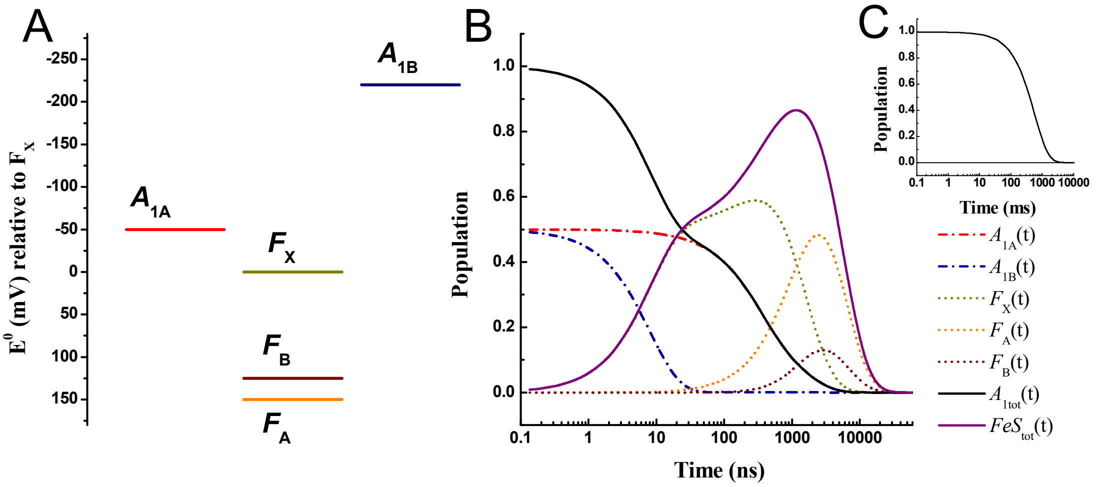

Figure 3. Panel A: reference energetic scheme for the "large driving force" scenario for A_1^- oxidation; standard redox potentials (E^0) are shown relative to F_X. **Panel B:** simulated population evolution of the individual redox active cofactors, $A_{1A}^-(t)$: dashed-dot red line, $A_{1B}^-(t)$ dashed-dot blue line, $F_X^-(t)$ dot golden line, $F_A^-(t)$ dot orange line, $F_B^-(t)$ dot burgundy line. Also shown are the total population evolutions of $A_{1,tot}^-(t) = A_{1A}^-(t) + A_{1B}^-(t)$ (black line) and $FeS_{tot}^-(t) = F_X^-(t) + F_A^-(t) + F_B^-(t)$ (purple line). The inset (**C**) shows the recombination kinetics simulated in absence of an exit from the system (k_{out} = 0). Temperature: 290 K.

The oxidation of A_{1B}^- is dominated by the 8.2 ns lifetime and that of A_{1A}^- by the 307 ns one, with some contribution from the 1,4 µs component. The proportion of fast:slow $A_{1,tot}^-$ oxidation phases are simulated as 0.5:0.5, corresponding to the initial populations of these cofactors. Different oxidation phase partitions could be straightforwardly simulated by setting the boundary conditions accordingly. This in turn implies an asymmetric charge separation/stabilisation between the two active ET chains of PSI (*e.g.* [20–24]). Discussion of this issue is however beyond the scope of this work. For equal initial population of $A_{1\mathrm{B}}^{-}$ and $A_{1\mathrm{A}}^{-}$, the resulting average lifetimes are 10.5 and 733 ns, respectively, and 371 ns for $A_{1,tot}^{-}$. The predicted oxidation of $A_{1\mathrm{A}}^{-}$ is somewhat slower, within this energetic scheme and for the conditions described, due to the significant contribution of the 1.4 µs phase, which exact value is in part linked to ET between the Fe-S clusters. Within this model, the reduction of F_{X} is multiphasic, with contributions from all the sub-microsecond components, *i.e.* 8.2, 295, 307 ns (Table 2), giving rise to an average rise lifetime of 143 ns, whereas F_{X}^{-} oxidation is largely dominated by the 1.4 µs phase, corresponding closely to the average oxidation (τ_{av}) time and the mean lifetimes of the population evolution (τ_{m}), being both 1.6 µs, and hence slower that 1.1 µs estimated for $A_{1,tot}^{-}$. As apparent form the inspection of the population evolutions (Figure 3B), in this energetic scenario, the oxidation of F_{X}^{-} clearly follows that of $A_{1,tot}^{-}$,whereas the two processes largely overlapped in the simulations performed within the small driving force energetic scheme (Figure 2B). This is associated to the slower rate of F_{A} reduction from F_{X}^{-} due to the larger reorganisation energy (1 eV rather than 0.7 eV). Although not necessarily impossible, it would be unusual that the reorganisation for an ET event between 4Fe-4S cluster were to be lower than the one associated to ET from phylloquinones to an iron-sulphur centre. For this reason, as well as to minimise the number of variable parameters, λ_{tot} was set to the same value. Simulations for different values of the reorganisation energy are however explored in Appendix S4 of the Supplementary Information where the effect of this parameter can be better appreciated.

Table 2. Rate-defining Parameters and Simulated ET kinetic for the large driving force energetic scenario.

Rate Determining Parameters							Electron Transfer Simulated Parameters						
							Amplitudes						
Reaction	X_{DA} (Å)	ΔG_{DA}^{0} (eV)	$\lambda_{t,DA}$ (eV)	$\bar{\omega}_{DA}$ (eV/ cm^{-1})	$k_{D\rightarrow A}$ (ns^{-1})	τ (ns)	$p_{A_{1\mathrm{A}}}$	$p_{A_{1\mathrm{B}}}$	$p_{F_{\mathrm{X}}}$	$p_{F_{\mathrm{A}}}$	$p_{F_{\mathrm{B}}}$	$p_{A_{1\mathrm{tot}}}$	$p_{FeS_{\mathrm{tot}}}$
$A_{1A}^{-}\rightarrow$	9.1	-0.05	1.0	0.022 (175)	0.00270	8.15	0.002	0.500	-0.504	0.0035	0.0000	0.501	-0.501
$A_{1B}^{-}\rightarrow$	9.0	-0.22	1.0	0.046 (375)	0.12249	294.7	0.0020	0.000	-0.003	0.3891	-0.550	0.002	-0.164
$F_{X}^{-}\rightarrow$	11.6	-0.15	1.0	0.034 (275)	0.00085	307.3	0.307	0.000	-0.414	-0.343	0.650	0.307	-0.107
$F_{A}^{-}\rightarrow$	9.5	0.025	1.0	0.034 (275)	0.00077	1411	0.187	0.001	0.912	-1.292	-0.468	0.188	-0.847
$F_{B}^{-}\rightarrow$	–	–	–	–	0.00100	4415	0.002	0.000	0.001	1.242	0.367	0.002	1.619

doi:10.20944/preprints202408.0661.v1

Summary of the parameters utilised for the simulations of forward electron transfer in reference PSI within the large-driving-force scenario for A_1^- oxidation. The rate-defining parameters which are common to all forward electron reactions are the electronic coupling matrix element, $|H_0|^2$=1.3 10^{-3} eV^2, the barrier camping factor β=1.34 Å^{-1} and the temperature T=290 K, which are defined in Equation 1 of the main text.

The tables also list the lifetimes (τ_i) and associated amplitudes (p_i) describing the population evolution of each of the cofactors described in the model. The total amplitude associated with the electron transfer kinetics of phylloquinones ($p_{A_{1\,\mathrm{tot}}}$) and iron-sulphur centres ($p_{FeS_{\mathrm{tot}}}$) are also presented in the table. The initial conditions for the amplitude simulations were $A_{1\mathrm{A}}^-(0) = A_{1\mathrm{B}}^-(0) = 0.5$ and zero on all other cofactors considered.

The terminal electron acceptors F_{A} and F_{B} are reduced with average lifetimes of 1.2 µs and 808 ns, respectively, and oxidised with average lifetimes of 3.4 and 1.8 µs respectively. The terminal acceptors oxidation is, basically, determined by the rate of exit from the system. The slower simulated dynamics of F_{A}^- oxidation are, as in the "weak driving force" scenario, due to considering a slightly endergonic reduction of F_{B}. Nonetheless, the mean lifetimes for F_{A}^- and F_{B}^- are 5.8 and 6.2 µs indicating that, as also discussed above, the two centres are predicted to be oxidised almost concertedly by diffusible acceptors.

When the rate of electron donation from F_{B}^- is suppressed in order to simulate the recombination reactions, these are characterised by a lifetime of ~570 ms, which falls rather outside the spread of values reported in the literature in which the slowest ones are in the order of 100 – 200 ms [6,26,68–71]. Yet, no specific effort has been made here to reach a good agreement between the measured and simulated recombination rates. An improvement in the match between modelled (between 174 and 89 ms) and experimental values is obtained by increasing $\hbar\bar{\omega}_{DA}$ to 55 meV (450 cm^{-1}) (Appendix S2, Figure S3), which is the average recommended consensus value from a survey in redox-active proteins [37]. Variation of the values of λ_{tot} (Appendix S3, Figure S6) or application of the parameter sets employed in the "weak driving force" model (Appendix S4, Figure S8), as discussed above, do not appear to improve the description of the recombination kinetics within the "large driving force" energetic scheme. Nonetheless, as in the "weak driving force" case, the recombination rate is limited by the uphill repopulation of F_{X}^- and, especially, $A_{1(\mathrm{A,B})}^-$. As discussed by Cherepanov and coworkers [**72**], a more detailed description of the Franck-Condon function, involving multiple nuclear modes and specific electron-phonon coupling terms, as well as explicit consideration of $A_{0(\mathrm{A,B})}^-$ (the up-stream electron donor) might be required to describe the recombination reactions in detail, at least within the large driving force energetic picture.

2.3. Effect of Changing the Driving Force of F_{X}^- *Oxidation* ($\Delta G^0_{F_{\mathrm{X}}\to F_{\mathrm{A}}}$)

The most straightforward change in PSI energetics that affects the ET between the iron-sulphur cluster directly, involves the tuning of the redox potential of the terminal electron acceptors F_{A} and F_{B}. Mutations in the PsaC subunit that modify the coordination, and hence the redox properties, of F_{A} and F_{B} have already been reported [73–84]. However, the effect of these mutations on the $A_{1\mathrm{A,B}}^-$ oxidation kinetics has not been investigated in details, since the main target of these studies was to identify the specific nature and coordination site of the terminal acceptor, which has been a matter of controversy before being definitely elucidated by the availability of high resolution structural models. Hence, these studies targeted primarily the residues directly involved in the binding of the FeS clusters [73–84], and the kinetic information reported related almost exclusively on the recombination rather than the forward ET reactions [73–82]. Similarly, mutants affecting either the direct coordination of F_{X} [85–88] and, in some cases, of nearby residues altering the cluster binding

doi:10.20944/preprints202408.0661.v1

niche [89–95], have also been produced. Actually, these mutants pioneered the application of site-directed mutagenesis to the study of PSI [85–87]. The main target of these studies was also the identification of the ligands and the interaction of the F_X -binding domain with the PSI acceptor side subunits. Most of these mutants resulted however in a loss or very low level of PSI accumulation, in centres lacking or having a heavily modified F_X centre [85–87] as well as in altered binding of PsaC and the neighbouring subunits [86–95]. This, in turn, restricted the possibility of studying the effect of the specific mutations on forward electron transfer, so that the characterisation of these modified reaction centres was then relatively limited [91–95]. Although mutants leading to the perturbations of the F_X properties are certainly interesting, these would lead to the simultaneous alteration of factors governing three ET events: the reduction of this cluster by both phylloquinones and its oxidation by F_A . Here, then, the discussion will be initially focused on changes in the redox potential of F_A ($E^0_{F_\mathrm{A}}$), since the $F_\mathrm{X} \rightarrow F_\mathrm{A}$ reaction follows immediately the phylloquinones in the ET cascade, but is not expected to modify the uphill reaction rates *directly*. Yet, any alteration in the F_A redox potential, leads to changes to both $\Delta G^0_{F_\mathrm{X} \rightarrow F_\mathrm{A}}$ and $\Delta G^0_{F_\mathrm{A} \rightarrow F_\mathrm{B}}$, albeit in the opposite direction, as the driving force for one reaction increase, the other decreases.

Figure 4 shows the simulated kinetics for all redox cofactors described in the energetic/kinetic model in which $E^0_{F_\mathrm{A}}$ was shifted by –25 mV (Figure 4A/B), –50 mV (Figure 4C/D) and –100 mV (Figure 4E/F), within the “weak driving force” scenario for phyllosemiquinone oxidation. For the –25 mV shift, F_A and F_B are isoenergetic, while for larger potential shifts the driving force for F_B reduction (by F_A) increases progressively, whereas that of F_A reduction by F_X^- decreases accordingly, but always remains favourable from a thermodynamic point of view.

doi:10.20944/preprints202408.0661.v1

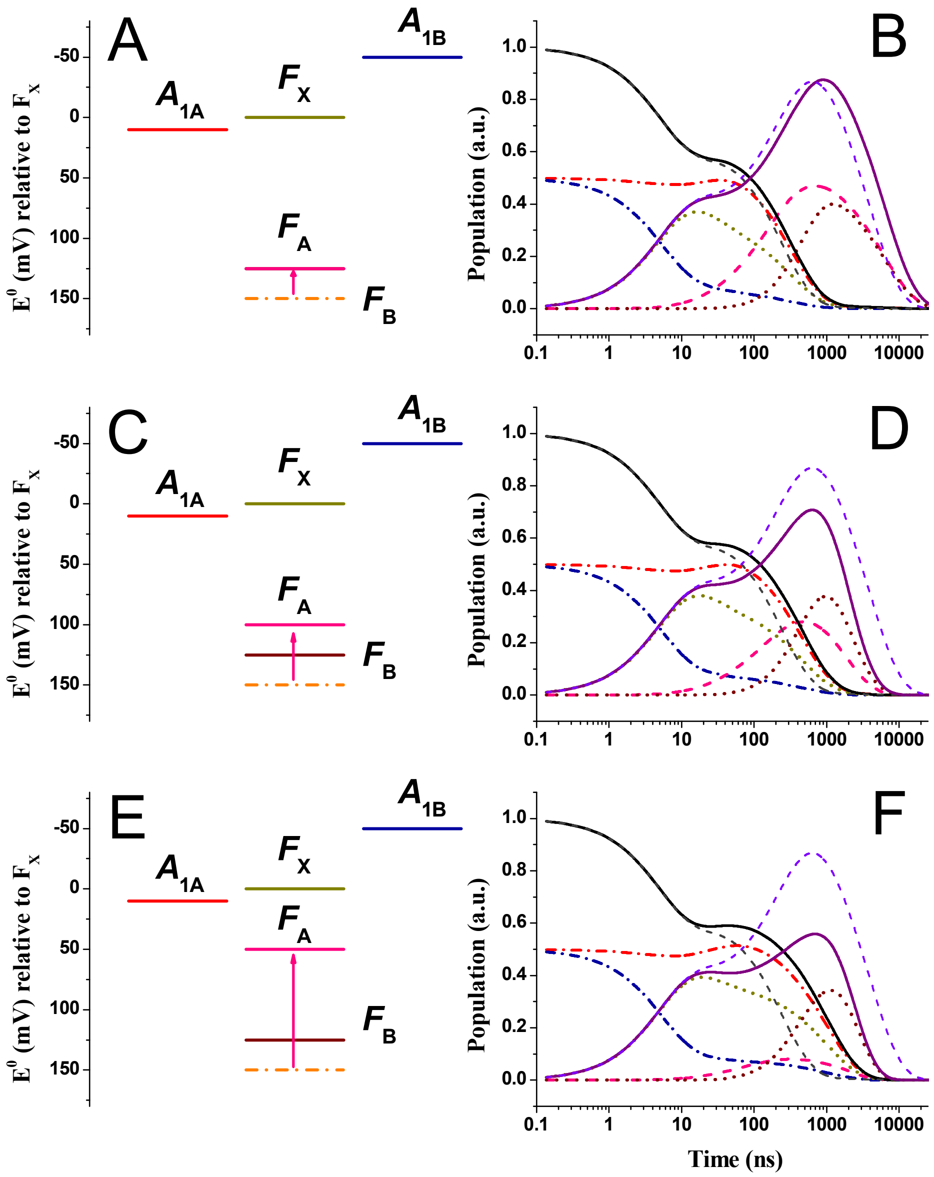

Figure 4. Panels A, C and **E:** energetic schemes showing the $E^0_{F_A}$ perturbations (altered value, pink line) with respect to the reference model being the "weak driving force" scenario for A_1^- oxidation. The reference $E^0_{F_A}$ potential is indicated by dashed-dotted orange lines. **Panel B, D** and **F:** simulated population evolution of the individual redox active cofactors, resulting from $E^0_{F_A}$ perturbations: $A_{1A}^-(t)$: dash-dot red line, $A_{1B}^-(t)$ dash-dot blue line, $F_X^-(t)$ dot golden line, $F_A^-(t)$ thick dash pink line, $F_B^-(t)$ dot burgundy line. The population evolutions of $A^-_{1,tot}(t)$ (black line) and $FeS^-_{tot}(t)$ (purple line) are also shown and compared with the simulation for the reference scenario (dash grey and violet lines for $A^-_{1,tot}(t)$ and $FeS^-_{tot}(t)$, respectively).

Figure 5 shows simulations for the same alterations of $E^0_{F_A}$, but within the "large driving force" phyllosemiquinone oxidation scheme.

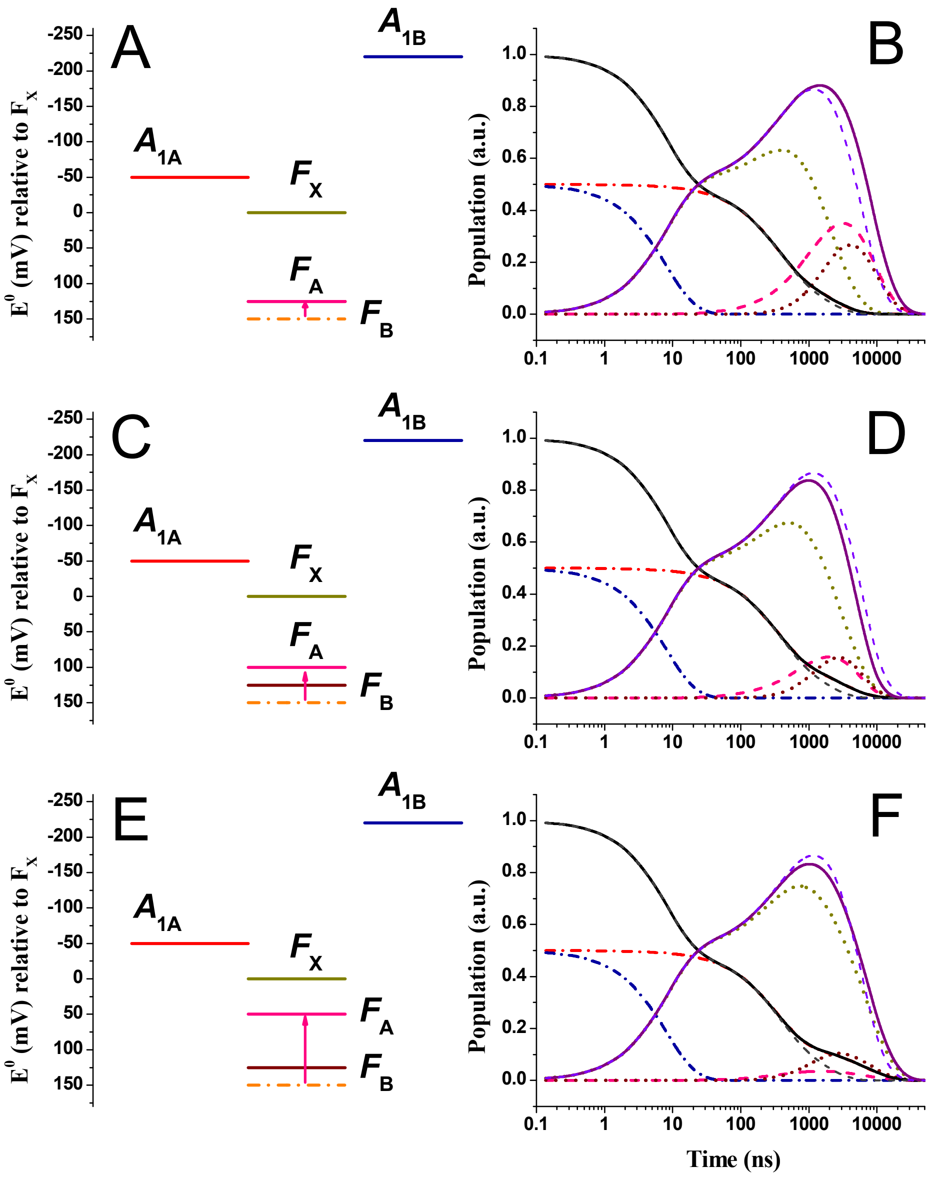

Figure 5. Panels A, C and E: energetic schemes showing the $E^0_{F_A}$ perturbations (altered value, pink line) with respect to the reference model being the "large driving force" scenario for A_1^- oxidation. The reference $E^0_{F_A}$ potential is indicated by dashed-dotted orange lines. **Panel B, D and F:** simulated population evolution of the individual redox active cofactors, resulting from $E^0_{F_A}$ perturbations: $A_{1A}^-(t)$: dash-dot red line, $A_{1B}^-(t)$ dash-dot blue line, $F_X^-(t)$ dot golden line, $F_A^-(t)$ thick dash pink line, $F_B^-(t)$ dot burgundy line. The population evolutions of $A_{1,tot}^-(t)$ (black line) and $FeS_{tot}^-(t)$ (purple line) are also shown and compared with the simulation for the reference scenario (dash grey and violet lines for $A_{1,tot}^-(t)$ and $FeS_{tot}^-(t)$, respectively).

The simulations of Figure 4 and Figure 5 show some significant differences in the ET kinetics when equal perturbations are applied to the driving forces of reactions which are otherwise described by, basically, the same parameters (Figure 2 and 3).

In the "weak driving force" scheme, together with the modification of the population evolutions of $F_{X,A,B}^-$, which are expected since the rate constants associated with these reactions are directly affected by the F_A redox potential perturbations, also significant alterations of the $A_{1,tot}^-$ oxidation kinetics are simulated (τ_{av,A_1^-} was 258, 360 and 840 ns vs. ~180 ns in the reference energetic scenario). This is particularly clear for the simulated A_{1A}^- kinetics, due to the increase in the value of the lifetime that dominates its oxidation, that is simulated as 340 and 530 ns and 1 µs for the $E_{F_A}^0$ perturbations discussed above vs 284 ns in the initial scenario. The kinetics of $A_{1,tot}^-$ oxidation became progressively slower as the rate of $F_X^- \rightarrow F_A$ became slower (7.2 x 10^{-3}, 5.9 x 10^{-3} and 2.1 x 10^{-3} ns^{-1} *vs.* 1 x 10^{-2} ns^{-1} in the starting scenario), because of the decrease in driving force, $\Delta G^0_{F_X \rightarrow F_A}$. However, irrespectively of the exact shift of the F_A redox potential, F_X^- reduction remained concerted with that of $A_{1,tot}^-$ and, on average, slowed down by the same extent (τ^d_{av,F_X^-} 326, ns 413 ns, 1 µs vs 199 ns in the reference system). On the other hand, F_A^- oxidation became progressively faster (as the potential of the cofactor became more reductive), and so did the oxidation of F_B^-, upon shifting from endergonic (Figure 2) to exergonic conditions (Figure 4). The maximal population of these cofactors decreased ($[F^-_{(X+A+B)}]^{max}$ 0.86, 0.70, 0.53 *vs.* 0.86 in the reference) with increased free energy for the last inter-protein ET step. The effect is clearly more pronounced for the maximal F_A^- reduction level ($[F_A^-]^{max}$ 0.45, 0.26 and 0.06 *vs.* 0.64 in the reference system).

Differently, in the "large driving force" scheme, the modifications of the F_A^- oxidation potential, together with the resulting changes in driving forces associated to the reactions in which this cofactor participates, appear to affect almost exclusively inter-Fe-S electron transfer reactions, whereas the kinetics of $A_{1,tot}^-$ oxidation remain almost unaffected (Figure 5). The only significant effect on A_1^- oxidation concerned the amplitude of a minor component displaying a long lifetime (~1.5 µs), which was also simulated for the reference system (Figure 3), but which value increased significantly upon $E_{F_A}^0$ perturbation (τ 3.7, 5.2 and 14 µs, respectively, *vs.* 1.4 µs in the reference system). The large value of this lifetime, even when having a small associated amplitude (<10% of total), has a marked impact on the estimation of τ_{av,A_1^-} (which was 680 ns, 875 ns and 2.2 µs in the F_A -perturbed *vs.* ~370 ns in the reference energetic system). It shall be recalled that this slow phase has never been detected experimentally, to the best of our knowledge. It is clearly connected to the explicit consideration of $F_A^- \rightarrow F_B$ reaction, as it is not simulated otherwise ([48,63,67] and Appendix S1, Table S1). Kinetic coupling in this scenario becomes significant since the rate of $F_X^- \rightarrow F_A$ transfer (8.8 10^{-4} ns^{-1}) is almost the same as that of $F_A^- \rightarrow F_B$ (7.7 10^{-4} ns^{-1}) and, especially, of the reverse, $F_B^- \rightarrow F_A$, reaction (1.5 10^{-4} ns^{-1}). This is not the case for the "weak driving force" scenario by virtue of the lower reorganisation energy (0.7 *vs.* 1 eV) required to describe the $A_1^- \rightarrow F_X$ and $F_X^- \rightarrow F_A$ reactions. Thus, when the µs-phase(s) is omitted from the calculations of τ_{av,A_1^-} in the "large driving force" simulations, the values of this parameter was almost unaffected by changes of $E_{F_A}^0$, varying from 122 ns in the reference system to 139 ns for the largest potential shift of –100 mV considered in the simulations of Figure 5.

Comparing Figure 4 and Figure 5, it can be appreciated that the effect of rendering F_A potential more reductive, is instead far more pronounced on the ET kinetics involving all iron-sulphur clusters in the case of the large driving force scenario for A_1^- oxidation. The cofactor showing the largest change in ET kinetic is F_X^-, which oxidation/reduction dynamics became progressively slower with average decay lifetimes of 3.8, 5.2 and 13 µs with respect to 2.7 µs in the reference system. When decreasing the driving force for F_X^- oxidation, its depopulation became progressively overlapped with that of $F_{A,B}^-$ and its maximal population increases from 0.59 in the reference system to 0.69, 0.72 and 0.79 as F_A becomes more reductive. The maximal cumulative population of the Fe-S clusters did not change significantly, indicating that the increase in transient F_X^- population level is accompanied by a parallel decrease in that of F_{A+B}^- (Figure 5).

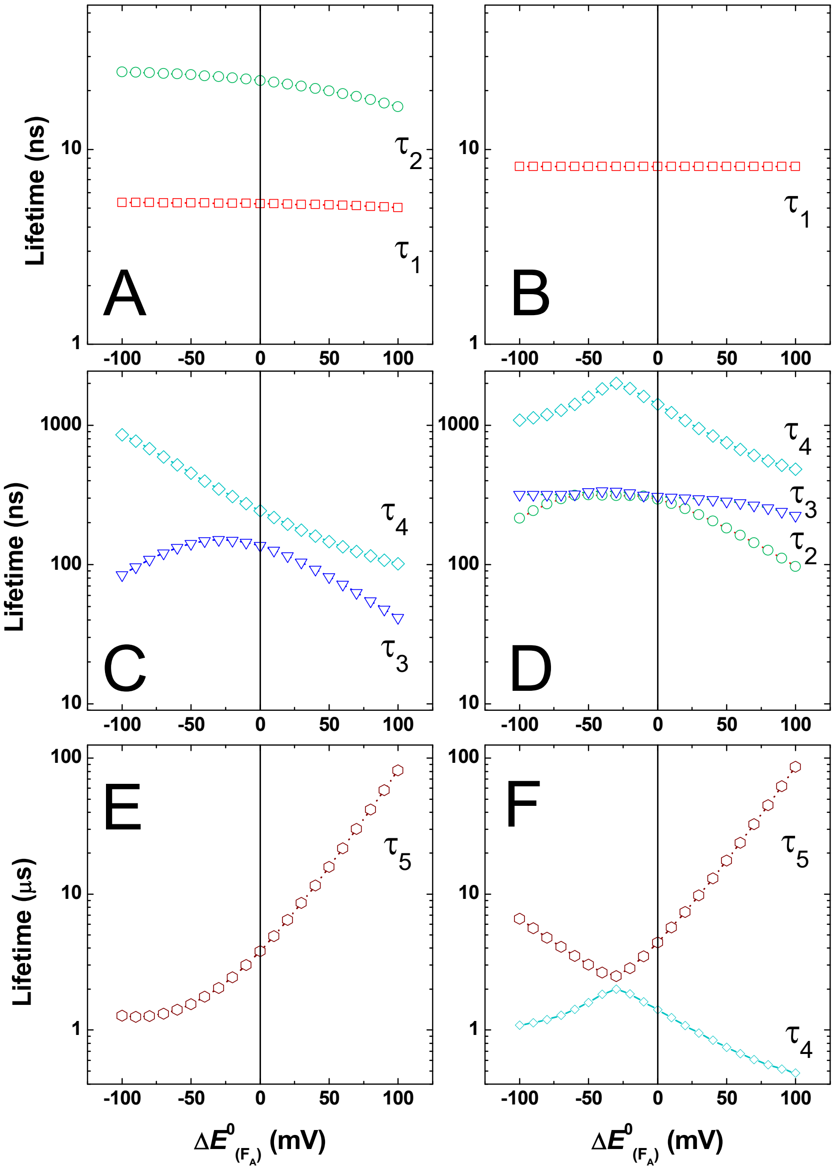

Figure 6. Simulated lifetimes resulting from variation of $E^0_{F_\mathrm{A}}$ (±100 meV), starting from the "weak" (**A, C, E**) and "large" (**B, D, F**) driving force models for A_1^- oxidation. **A, B**: $\tau < 50$ ns; **C, D**: 50 ns< $\tau < 1$ µs; **E, F:** $\tau >1$ µs. τ_1: red squares; τ_2: green circles; τ_3: blue triangles; τ_4: cyan diamonds; τ_5: burgundy hexagon. In panel **F**, τ_4 (cyan diamonds) is re-plotted to facilitate comparison with τ_5.

To obtain a more comprehensive picture of the effect resulting from perturbations of the F_A redox potential, and in turn the $\Delta G^0_{F_\mathrm{X}\to F_\mathrm{A}}$ and $\Delta G^0_{F_A\to F_B}$ free energies, the value of $E^0_{F_\mathrm{A}}$ was changed in ±100 mV interval with respect to the reference systems. The effect of tuning the $E^0_{F_\mathrm{A}}$ redox potential on the simulated lifetimes is presented in Figure 6 starting from the initial reference being either the "weak" (Figure 6A, C and E) or "large" driving force (Figure 6B, D, F) energetics for A_1^- oxidation. In Figure 6, lifetimes values were separated in classes for ease of presentation and comparison, so that Figure 6A and B show τ <~50 ns, Figure 6C and D show ~50 ns< τ <~1 µs and Figure 6E and F, τ >~1 µs. Since the lifetimes change upon F_A perturbation, this classification is not strict, but refers to the dominant behaviour of a given lifetime component. The values of τ <50 are

doi:10.20944/preprints202408.0661.v1

not greatly affected by any perturbation of $E^0_{F_\mathrm{A}}$ in the ±100 mV interval considered. These lifetimes, τ_1 and τ_2 in the reference weak-driving force and τ_1 only in the reference large-driving force energetic scheme, reflect principally $A^-_{1\mathrm{B}}$ oxidation, that is exergonic in both. The simulated kinetics of Figure 4 and 5 show the prediction of little alterations in this kinetic phase when modifying successive ET reactions.

For lifetime values in the 50 ns< τ <~1 μs range (Figure 6C and D), starting-model-dependent variations are predicted instead. In the starting weak-driving force case, A^-_{1A} oxidation is dominated by the value of τ_4, which simulated values increase with the increase of $\Delta G^0_{F_\mathrm{X}\to F_\mathrm{A}}$, *i.e.* with the lowering of the reaction driving force (Figure 6C). The τ_3 lifetime in this energetic configuration, relates principally to ET reactions amongst the Fe-S clusters and its reference value of ~160 ns is an agreement with experimental estimation [30,33,34]. Its dependence from the variation of F_A redox potential is not monotonic, consistent with it being determined by the kinetic coupling of reactions influenced by both $\Delta G^0_{F_\mathrm{X}\to F_\mathrm{A}}$ and $\Delta G^0_{F_\mathrm{A}\to F_\mathrm{B}}$.

In the starting large-driving force energetic scheme, $A^-_{1\mathrm{A}}$ oxidation is dominated by the value of τ_3 instead, which is close to independent from the redox potential of F_A. As discussed for the simulations of Figure 5, the two main phases of A^-_1 oxidation remain largely unaffected by perturbing $E^0_{F_\mathrm{A}}$, even in the large ± 100 mV range, within this reference scenario (Figure 6D), consistently with the phylloquinone oxidation being (mainly) kinetically decoupled from the successive ET steps. For this initial energetic configuration, τ_2 displays a dependence to $E^0_{F_\mathrm{A}}$ variation similar to the one simulated for τ_3 in the weak-driving force model, albeit its starting value is somewhat larger (~250 ns, this is because of the slightly larger value of λ_{tot}, *i.e.* 1 eV *vs.* 0.9 eV). This component shall then also be taken as reflecting principally transfer between Fe-S clusters. Since it is not simulated when not considering F_A and F_B explicitly ([48] and Appendix S1), it most likely reflects ET transfer between the terminal acceptors. This simulated lifetime is in general agreement with the inter 4Fe-4S clusters electron transfer estimated by Nuclear Magnetic Resonance methods in the ferredoxin of *Chromatium vinosum* (~300 ns) which is structurally analogous to the PsaC subunit [96]. The value of τ_4 is also larger in the reference large driving scheme with respect to the weak-driving force configuration. Its initial value of ~1 μs is the same as the one simulated when F_A and F_B are not explicitly taken into account ([48] and Appendix S1) and therefore reflects mainly F^-_X oxidation. This lifetime shows a non monotonic dependence on $E^0_{F_\mathrm{A}}$, with an apparent discontinuity point at –40 mV potential shift (Figure 6D), which is for a decrease of F^-_X oxidation driving force (less exergonic) and an increase in the driving force (more exergonic) for F^-_A oxidation by F_B.

Different behaviour with respect to shifts in the $E^0_{F_\mathrm{A}}$ value are also simulated for the slowest lifetime (τ_5). In the reference weak-driving force A^-_1 oxidation, τ_5 shows a quasi-monotonic dependence, becoming faster as the driving force for F^-_A oxidation by F_B increases. For the largest favourable energetic configuration the value of this lifetime approaches the inverse of the out-put from the system k^{-1}_{out} ~1 μs (Figure 6E). In the large-driving force A^-_1 oxidation framework, τ_5 has a more complex dependence, with the lifetime also becoming faster for increased $F^-_\mathrm{A}\to F_\mathrm{B}$ oxidation driving forces. However, similarly to τ_4, which is also re-plotted in Figure 6F for direct comparison, a trend discontinuity point at ~ –40 mV potential shift is simulated. Under these energetic conditions, the decrease in driving force for F^-_X oxidation dominates over the increased driving force for the successive ET steps.

In both cases, the slowest values simulated, especially for conditions in which $F^-_\mathrm{A}\to F_\mathrm{B}$ is significantly endergonic, indicates that the equilibration between the terminal electron acceptors can significantly slow down ET to the diffusible acceptors carries (*e.g.* ferredoxin). A slow $F^-_\mathrm{X}\to F_\mathrm{A}$ ET reaction would have similar consequences, as shown by the τ_5 dependence of Figure 6F as well as the simulations of Figure 4. The latter effect, to our knowledge has not previously been explicitly considered, whereas it might have important implications for the photosystem functionality.

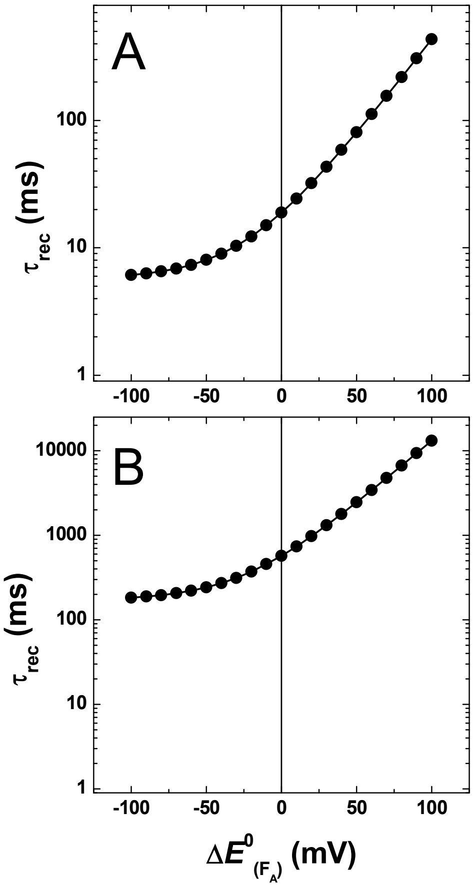

Figure 7. Simulated recombination lifetimes resulting from variation of $E^0_{F_A}$ (±100 meV), starting from the "weak" (**A**) and "large" (**B**) driving force models for A_1^- oxidation.

Figure 7 shows the dependence on the simulated recombination reactions, *i.e.* when $k_{out} = 0$. In both energetic scenarios, the lifetime for charge recombination displays a positive correlation with the increase in driving force for the $F_X^- \to F_A$ reaction. For values of $E^0_{F_A}$ that yields $\Delta G^0_{F_A \to F_B} < 0$ (*i.e.* ~< –25 mV shift) the recombination lifetime depends only weakly on the exact value of $\Delta G^0_{F_X \to F_A}$. Yet, as the $F_A^- \to F_B$ transfer enters the endergonic regime ($\Delta G^0_{F_A \to F_B} >> 0$), the recombination lifetimes display almost an exponential response with respect to the decrease of $\Delta G^0_{F_X \to F_A}$, *i.e.* an increase in driving force for the forward and a decrease of backward reactions, in agreement with back-population of F_X^- imposing important kinetic limitation to these recombination reactions.

2.4. Effect of Changing the Driving Force of F_A^- Oxidation ($\Delta G^0_{F_A \to F_B}$)

The driving force for F_A^- oxidation can be modulated, without directly affecting the energetics of F_X^-, by modifying the redox potential of F_B ($E^0_{F_B}$).

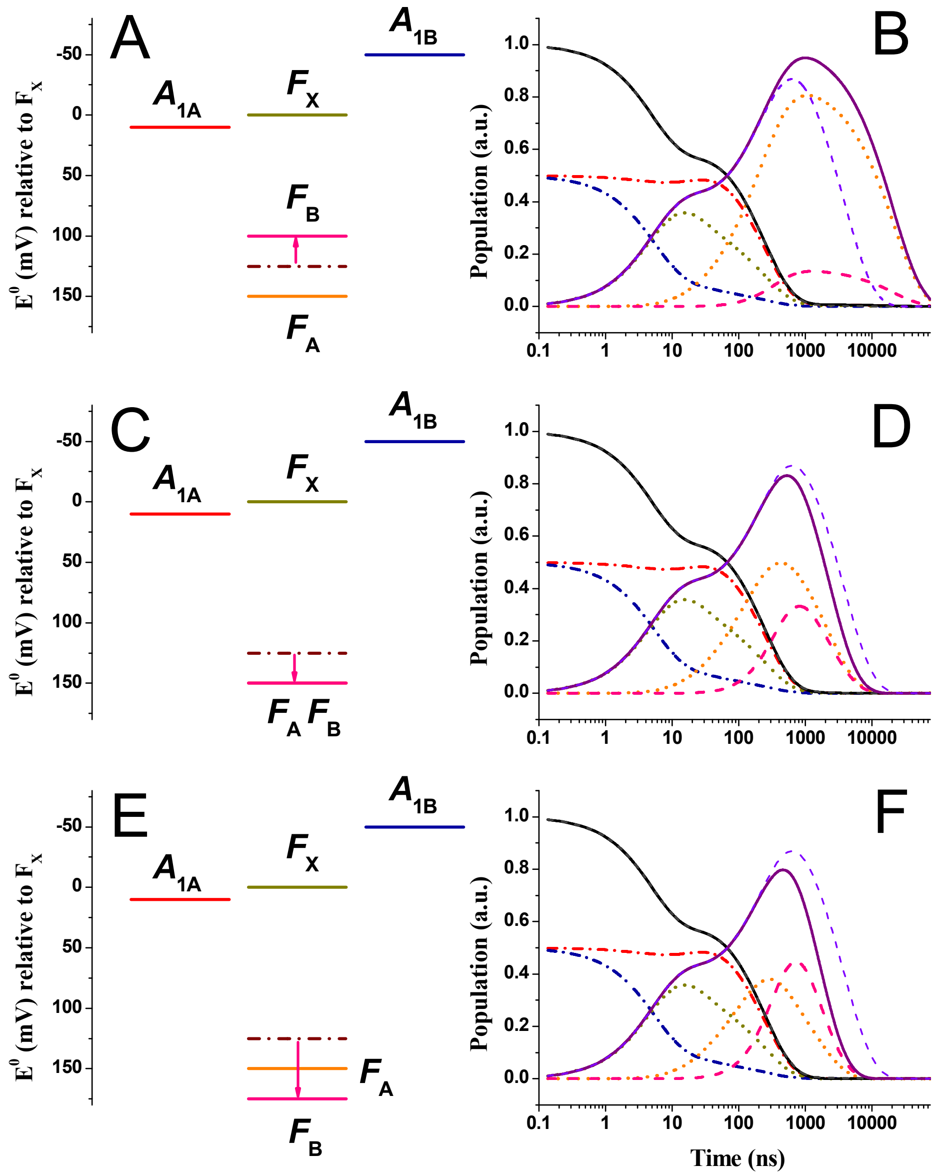

Figure 8. Panels A, C and E: energetic schemes showing the $E^0_{F_\mathrm{B}}$ perturbations (altered value, pink line) with respect to the reference model being the “weak driving force” scenario for A_1^- oxidation. The reference $E^0_{F_\mathrm{B}}$ potential is indicated by dashed-dotted burgundy lines. **Panel B, D and F:** simulated population evolution of the individual redox active cofactors, resulting from $E^0_{F_\mathrm{B}}$ perturbations: $A_{1\mathrm{A}}^-(t)$: dash-dot red line, $A_{1\mathrm{B}}^-(t)$ dash-dot blue line, $F_\mathrm{X}^-(t)$ dot golden line, $F_\mathrm{A}^-(t)$ dot orange line, $F_\mathrm{B}^-(t)$ thick dash pink line The population evolutions of $A_{1,tot}^-(t)$ (black line) and $FeS_{tot}^-(t)$ (purple line) are also shown and compared with the simulation for the reference scenario (dash grey and violet lines for $A_{1,tot}^-(t)$ and $FeS_{tot}^-(t)$, respectively).

Figure 8 (“weak driving force” energetics) and Figure 9 (“large driving force” energetics) show the simulated kinetics of all redox cofactors considered in the models, upon shifting the F_B potential by +25 mV (Figure 8/9B), –25 mV (Figure 8/9D) and –50 mV (Figure 8/9F). In this case, for the +25 mV shift, $F_\mathrm{A}^- \rightarrow F_\mathrm{B}$ becomes more endergonic ($\Delta G^0_{F_\mathrm{A}\rightarrow F_\mathrm{B}}$ = +50 meV), for the –25 mV $E^0_{F_\mathrm{B}}$ shift F_A and F_B are isoenergetic ($\Delta G^0_{F_\mathrm{A}\rightarrow F_\mathrm{B}}$ = 0 meV), and for the –50 mV shift F_A^- oxidation is exergonic (

doi:10.20944/preprints202408.0661.v1

$\Delta G^0_{F_A\rightarrow F_B}$ = –25 meV). The impact of exploring a ±100 mV variation of $E^0_{F_B}$ on the lifetimes describing ET in PSI is shown in Figure 10.

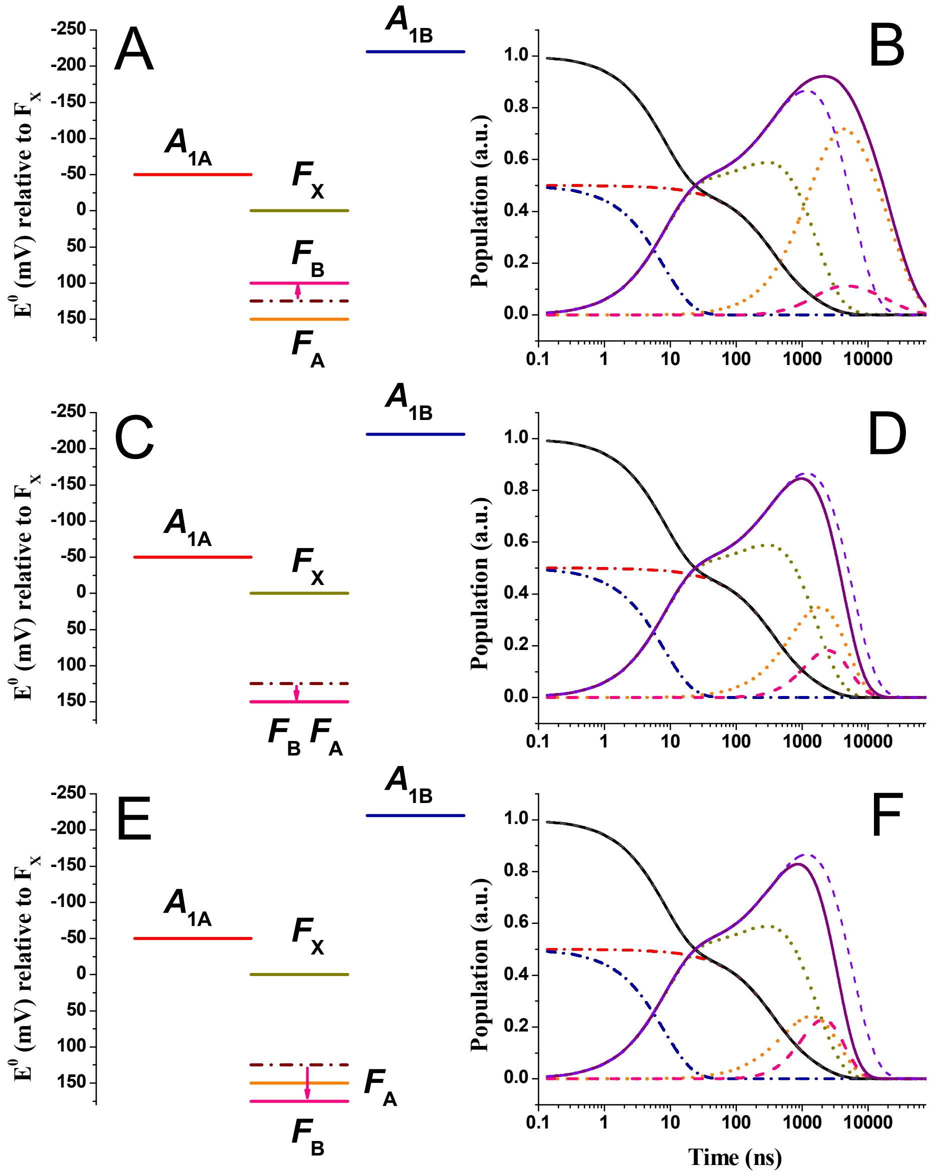

Figure 9. Panels A, C and E: energetic schemes showing the $E^0_{F_B}$ perturbations (altered value, pink line) with respect to the reference model being the "large driving force" scenario for A_1^- oxidation. The reference $E^0_{F_B}$ potential is indicated by dashed-dotted burgundy lines. **Panel B, D and F:** simulated population evolution of the individual redox active cofactors, resulting from $E^0_{F_B}$ perturbations: $A_{1A}^-(t)$: dashed-dot red line, $A_{1B}^-(t)$ dashed-dot blue line, $F_X^-(t)$ dot golden line, $F_A^-(t)$ dot orange line, $F_B^-(t)$ thick dash pink line The population evolutions of $A_{1,tot}^-(t)$ (black line) and $FeS_{tot}^-(t)$ (purple line) are also shown and compared with the simulation for the reference scenario (dash grey and violet lines for $A_{1,tot}^-(t)$ and $FeS_{tot}^-(t)$, respectively).

Comparison of the simulations presented in Figures 8 and 9 indicates that, irrespectively of the reference energetic model utilised to describe A_1^- oxidation, alterations affecting selectively $\Delta G^0_{F_A\rightarrow F_B}$ do not impact on the phyllosemiquinone oxidation kinetics, as they are, in both cases, basically indistinguishable from the respective reference system. The same hold true for wider changes in $E^0_{F_\mathrm{B}}$ of ± 100 mV, since the values of τ_1, τ_2, and τ_4 (Figure 10A and C), which dominates A_1^- oxidation in the "weak" driving force scenario, are barely affected by changes in $\Delta G^0_{F_\mathrm{A}\to F_\mathrm{B}}$. The same is observed for τ_1 and τ_3 that dominates A_1^- oxidation in the large-driving force A_1^- oxidation framework (Figure 10B and D). The value of the τ_4 which is also associated with a small-amplitude-µs A_1^- oxidation phase in this energetic configuration, barely depends on $\Delta G^0_{F_\mathrm{A}\to F_\mathrm{B}}$. On the other hand, as expected, changing $\Delta G^0_{F_\mathrm{A}\to F_\mathrm{B}}$ affects the kinetics of electron transfer between the Fe-S clusters, especially the temporal evolutions of F_A^- and F_B^-, whereas that of F_X^- is only slightly perturbed. In brief, the overall reduced population of F_A increased with the decrease in driving force for its oxidation by F_B, and vice versa, so that with the decrease of $\Delta G^0_{F_\mathrm{A}\to F_\mathrm{B}}$ the temporal evolution of the reduced state of this cofactors became less concerted and, basically, sequential for large driving forces.

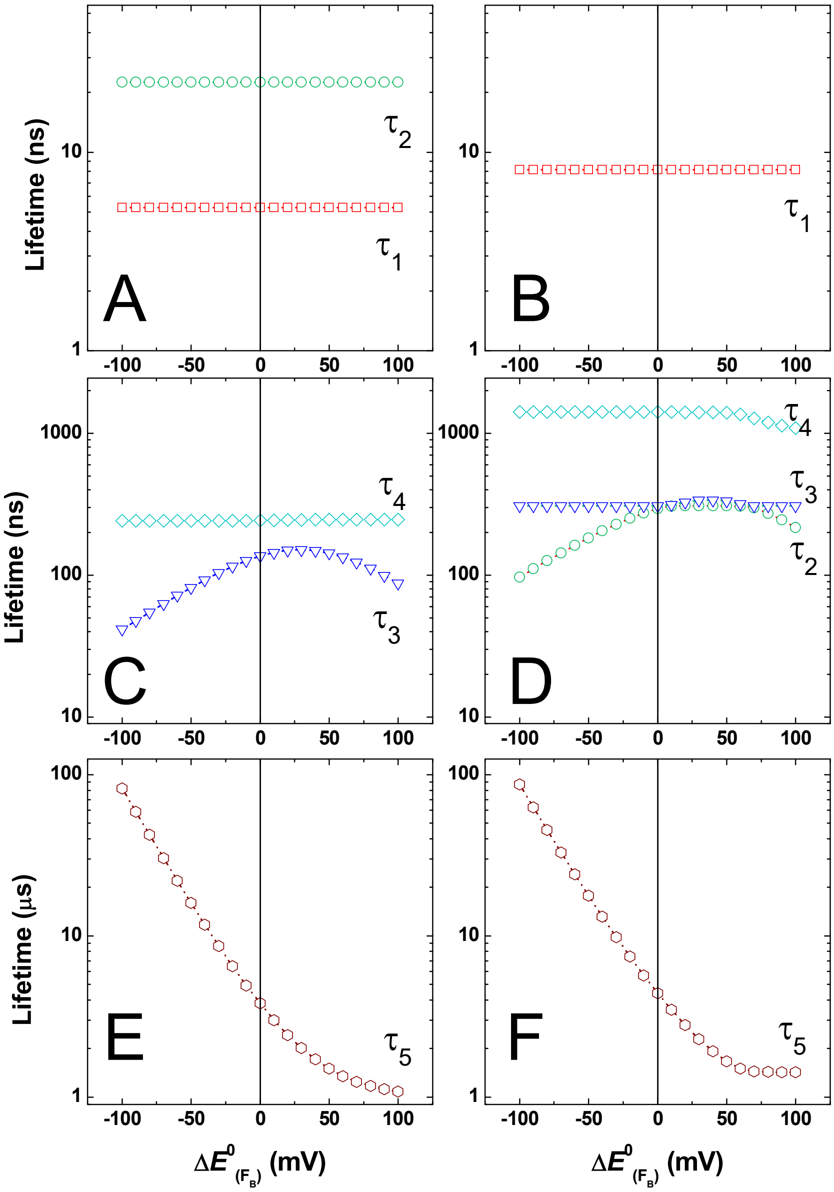

Figure 10. Simulated lifetimes resulting from variation of $E^0_{F_\mathrm{B}}$ (±100 meV), starting from the "weak" (**A, C, E**) and "large" (**B, D, F**) driving force models for A_1^- oxidation. **A, B**: $\tau < 50$ ns; **C, D**: 50 ns<

$\tau < 1$ μs; **E, F:** $\tau > 1$ μs. τ_1 : red squares; τ_2 : green circles; τ_3 : blue triangles; τ_4 : cyan diamonds; τ_5 : burgundy hexagon.

Interestingly, the values of τ_3 ("weak driving force" reference energetics, Figure 10C) and τ_2 ("large driving force" reference energetics, Figure 10D) show a non-monotonous dependence on variation of $\Delta G^0_{F_A \to F_B}$, with the slowest values simulated, in both cases, upon F_A and F_B becoming close to iso-energetic. These behaviours are similar to those simulated for variations in the $E^0_{F_A}$, which also affected $\Delta G^0_{F_A \to F_B}$.

The lifetime showing the greatest dependence on $E^0_{F_B}$ is the one representing the *effective* exit from the system (τ_5). An almost monotonous decrease (decay deceleration) is predicted upon progressive decreasing $\Delta G^0_{F_A \to F_B}$, for values of $E^0_{F_B}$ under which the $F_A^- \to F_B$ reaction falls in the endergonic regime. A softer dependence is simulated instead for the large exergonic regimes, *i.e.* for F_B potential shifts >~60–80 mV (Figure 10 E/F). Under the latter conditions, the value of τ_5 (at least in the weak-driving force scenario) approaches that of k_{out}^{-1} (~1 μs).

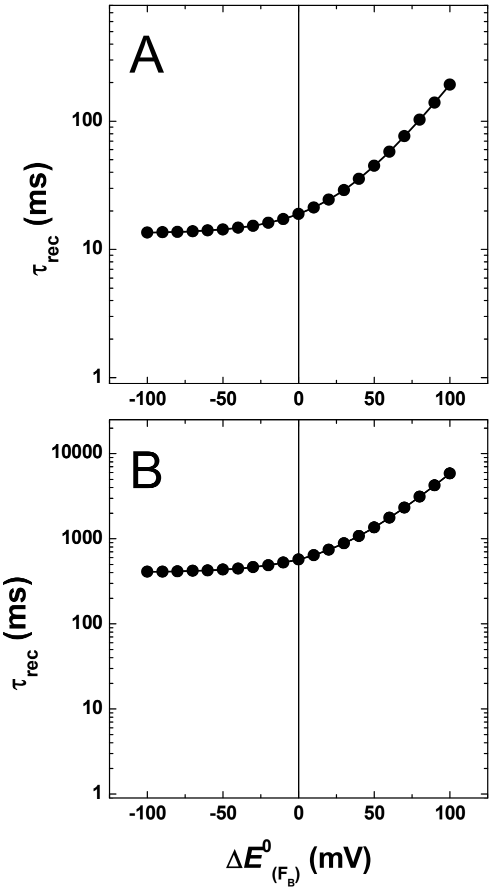

Figure 11. Simulated recombination lifetimes resulting from variation of $E^0_{F_B}$ (±100 meV), starting from the weak (**A**) and large (**B**) driving force models for A_1^- oxidation.

Figure 11 shows the simulated recombination in the absence of an exit from the system. Irrespectively of the energetics associated to A_1^- oxidation, the kinetics of charge recombination displayed a weak dependence on $\Delta G^0_{F_A \to F_B}$, maintaining the value simulated for the reference scenario, for shifts in $E^0_{F_B}$ of less than about ~60 mV. A significant increase is however predicted when $F_A^- \to F_B$ enters the large endergonic regime, $\Delta G^0_{F_A \to F_B}$ > 60 mV. The overall response of charge recombination kinetics is similar, but less pronounced, than the one predicted upon perturbations of $E^0_{F_\mathrm{A}}$, that affects both $\Delta G^0_{F_\mathrm{A} \to F_\mathrm{B}}$ and $\Delta G^0_{F_X \to F_A}$ (Figure 7), albeit in contrasting fashion. This indicates that, although the repopulation of F_X^- imposes the largest kinetic limitations to charge recombination, back-population of F_A^- will also slow this reaction when its oxidation by F_B becomes largely favourable.

3. Materials and Methods

Kinetic simulations were performed as described previously **[12,48,49]**. In brief the population evolutions of the redox cofactors considered in the kinetic model (as schematically shown in **Figure 1**) are obtained from solving a system of ordinary differential equations, which in compact matrix form, is defined by $\dot{\mathbf{P}}(t) = \mathbf{K}_i \cdot \mathbf{P}(t)$. $\mathbf{P}(t)$ and $\dot{\mathbf{P}}(t)$ are the vectors describing the temporal evolution of the redox cofactors populations and its first derivative, respectively, and $\mathbf{K}_i$ is a square matrix, frequently referred to as the rate matrix, that has as its elements the *rate constants* between pairs of electron donors and acceptors. The index *i* corresponds to the number of cofactors (states) considered in the modelling. The system of linear differential equation has a general solution of the form: $\mathbf{P}(t) = \sum_{J=1}^{i} c_j \mathbf{V}_j e^{\zeta_j t}$, where ζ_j and $\mathbf{V}_j$ are, the eigenvalues and the eigenvectors, respectively, that diagonalise the matrix $\mathbf{K}_i$, and c_j are a set of scalars that need to be determined according to some given initial conditions, that were here considered to be: $A_{1\mathrm{A}}^-(0) = A_{1\mathrm{B}}^-(0) = 0.5$ and $F_\mathrm{X}(0) = F_\mathrm{A}(0) = F_\mathrm{B}(0) = 0$. The general solution of the system corresponds to the empirical linear combination of weighted exponentials frequently employed to describe the experimental kinetics. Thus, the eigenvalues, that are univocally determined by the eigen-decomposition of $\mathbf{K}_i$ reflect in the experimentally observed lifetimes ($\tau_{j,obs}$) through the relation $\tau_{j,obs} = -\zeta_j^{-1}$. The product $c_j \mathbf{V}_j$ relates only indirectly to the experimental pre-exponential amplitudes. The modelled amplitudes represent "weighted" molar fractions, and describe only the changes in the relative cofactor concentration over time, whereas the experimental values are also determined by the monitored properties of the cofactors (*e.g.* the wavelength-dependent extinction coefficient, fluorescence yield/spectra, and so on).

The link with theory is provided by using explicitly a physical description of the rate constants rather than setting their values as free simulation parameters. To this end, here we adopted the description between a pair of donor-acceptor molecules, originally derived by Hopfield **[36,65]**, when considering a single (mean) nuclear mode coupled to the ET event:

$$k_{D \to A} = \frac{2\pi}{\hbar} \left| H_{DA} \right|^2 \frac{1}{\sqrt{2\pi\sigma^2}} e^{-\frac{(\Delta G^0_{DA} + \lambda_{tot})^2}{2\sigma^2}}$$
$$\sigma^2 = \lambda_{tot} \hbar \bar{\omega} \coth \frac{\hbar \bar{\omega}}{2 k_B T} \qquad \text{Equation 1}$$

Where λ_{tot} is the total reorganisation energy, $\bar{\omega}$ is the angular frequency of the mean coupled nuclear mode, $\hbar$ is the Dirac constant, k_B is the Boltzmann constant, T is the temperature and $\left| H_{DA} \right|^2$ is the electronic coupling term, which can be to a good level approximated as $\left| H_{DA} \right|^2 = \left| H_0 \right|^2 e^{-\beta (X_{DA} - 3.6)}$ where $\left| H_0 \right|^2$, is the maximal value of the electronic coupling at wavefunctions overlap; β, a damping term associated to the probability of tunnelling the potential barrier, X_{DA}, the edge-to-edge cofactor distance (in Å) and 3.6 represents a correction for the van der

Waals radii. When $\hbar\bar{\omega} << k_B T$, $\sigma^2 = 2\lambda k_B T$ and the expression therefore simplifies, yielding the semi-classical relation derived by Marcus **[35]**.

In the presented simulations values of $|H_0|^2$ ~1.3 10^{-3} eV^2 (*e.g.* [48,49]) and β=1.38 Å^{-1} [**37**] were considered. Specific values of ΔG^0_{DA}, $\hbar\bar{\omega}$ and λ_{tot} will be discussed below.

It is often convenient to compare the average (τ_{av}) and mean (τ_m) lifetime obtained from the simulations, rather than comparing the individual pre-exponential amplitudes (p_i) and lifetimes. These parameters are defined, for each of the level (cofactor) considered, as:

$$\tau_{av} = \frac{\sum_i p_i \tau_i}{\sum_i p_i} \qquad \text{Equation 2}$$

Since the sum at the denominator is zero for all cofactors which have no initial population, two other derived parameter associated to it are considered for these cofactors, the average rise (τ^r_{av}) and depopulation (τ^d_{av}) lifetimes. These are obtained by performing the summations in Eqn. 2 considering only the pre-exponential having negative (p_{i-}) or positive (p_{i+}) amplitudes, respectively.

The mean lifetimes represent the first moment of the population evolution, that being described by a linear combination of exponential is defined for each cofactors as:

$$\tau_m = \frac{\sum_i p_i \tau_i^2}{\sum_i p_i \tau_i} \qquad \text{Equation 3}$$

which is always defined irrespectively of the initial amplitudes of the cofactors.

4. Conclusions

In this work the effect of altering the redox potential of the terminal acceptors of PSI, the iron-sulphur clusters, F_{A} and F_{B}, has been explored employing theory-based kinetic model simulations. This approach allows to predict the electron transfer kinetics between the Fe-S clusters, which has proven cumbersome to address experimentally by spectroscopic methods because of the characteristics of these cofactors and because of the spectral crowding occurring in large chromophore-pigment super-complexes, like PSI. The effect of altering F_{A} and F_{B} redox reactivity was comparatively explored by considering two energetic scenarios for ET reactions involving the upstream redox cofactors, the iron-sulphur cluster F_{X} and the phylloquinones $A_{1\mathrm{A}}$ and $A_{1\mathrm{B}}$, as the latter are better characterised by time-resolved spectroscopic approaches. From the presented analysis it is possible to infer that:

i) tuning the F_{A} redox potential, together with an alteration of the ET kinetics directly involving this redox centre, also affects the phyllosemiquinones oxidation kinetics, particularly of the slow kinetic phase of this process that is dominated by the depopulation of $A^-_{1\mathrm{A}}$. Significant kinetic perturbations are predicted within the "weak driving force" scenario for A^-_1 oxidation by F_{X}. Tuning $E^0_{F_{\mathrm{A}}}$ has instead a limited effect on A^-_1 oxidation kinetics when considering the "large driving force" energetic scheme for these cofactors oxidation reactions. Since both energetic schemes describe adequately several measured parameters, they can both be considered realistic. A more in-depth analysis of mutants affecting F_{A} coordination in the PsaC subunit, some of which have already been reported (*e.g.* [73–84]) but not studied with sufficient (ns) temporal resolution, is expected to shed further light on the energy gap between $A_{1(\mathrm{A/B})}$ and F_{X}, especially since the redox potential of the modified F_{A} cofactor shall be accessible by direct electrochemistry and henceforth correlated to the kinetic perturbation. Similar approaches have already been explored and proven feasible (*e.g.* [75–77]) yet, as already discussed, the effect of the mutations on the kinetics of forward ET reactions has not investigated in detail yet.

ii) tuning the F_{B} redox potential is predicted to affect almost exclusively ET involving the iron-sulphur clusters instead, especially the oxidation kinetics of F_A^- and F_B^-, without significantly impacting on the A_1^- oxidation kinetics, irrespectively of the energetic scenario employed to describe the latter reaction.

iii) alterations of the F_{B} redox potential, which are also been reported for mutants affecting its coordination site in the PsaC subunit (*e.g.* [73–84]), can however help in elucidating the actual energetics of ET between the terminal iron-sulphur clusters, which might be inferred from differences in both the recombination rates and forward ET to ferredoxin, in comparison with similar perturbation of the F_{A} redox potential.

iv) the ~180-ns kinetic phase experimentally retrieved in investigations of A_1^- oxidation kinetics [30,33,34,62,63], appears to be associated principally with F_{A}^- oxidation by F_{B}, whereas it was previously assigned to F_{X}^- oxidation by F_{A} [30]. The ~180-ns lifetime appears as a significant contribution also in the F_{X}^- oxidation kinetics, indicating that F_{A}^- oxidation by F_{B} is not fully kinetically decoupled from upstream reactions. This lifetime is correctly predicted in the “weak driving force” A_1^- oxidation scenario, whereas a slight overestimation (~300 ns) is obtained in the “large driving force” energetic scheme.

v) the need to consider λ_{tot} ~ 1 eV in the large driving force A_1^- oxidation scenario led to simulate a relatively slow F_{X}^- oxidation, which couples to a small-amplitude $A_{1\mathrm{A}}^-$ oxidation phase in the μs windows. This phase has not been detected experimentally either because not present or not resolvable. Multiple pieces of evidence suggest that F_{X}^- oxidation shall proceed in the sub-μs scale. This can be taken as an indication that λ_{tot} ~ 1 eV represents an upper limit/overestimation of this parameter. The calculated recombination rates, which are limited by the back-population of F_{X}^-, argues in the same direction, as they are overestimated, in general, by about an order of magnitude within the “large driving” force scenario (see Appendixes S2 and S3 for further discussion and simulations).

vi) uphill ET from F_{A}^- to F_{B} can significantly slow down donation from the terminal electron acceptor(s) to diffusible carriers, at least when pre-bound complexes are formed, *i.e.* the speed of electron transfer to ferredoxin (or other acceptors) might not depend solely on the rate of transfer from F_{B}^- to the redox active centre in the acceptor molecules, particularly if the intrinsic rate constant for this reaction is as-fast-as, or comparable with, the electron transfer kinetics involving the terminal electron acceptors within the photosystem..

Supplementary Materials: The supplementary information are organised in appendixes proving additional information concerning the reference schemes for the “weak driving force” and “large driving force” scenario, which serve as the basis to explore perturbations of the physical-chemical properties of the iron-sulphur cluster F_{A} and F_{B}. In Appendix S1 is shown a comparison of model simulations for a three-cofactor model, comprising only $A_{1\mathrm{A}}$, $A_{1\mathrm{B}}$ and F_{X} with respect to the reference five-cofactor models used in the main text (Figure S1 and Table S1). Also presented in this appendix are simulations performed omitting all recombination reactions to P_{700}^+ or leaving only the recombination between $A_{1\mathrm{A/B}}^-$ and P_{700}^+. In the latter case also the recombination kinetics in the absence of an exit from F_{B} are simulated (Figure S2). In Appendix S2 is shown a comparison of both forward and recombination kinetics when increasing the frequency of the mean coupled mode to the electron transfer reactions in the two reference energetic/kinetic schemes. Two parameter sets are used, in one case $\hbar\bar{\omega}_{DA}$ = 55 meV (450 cm^{-1}) is considered for all reactions including $A_{1\mathrm{A/B}}^-$ oxidation, in the other $\hbar\bar{\omega}_{DA}$ = 55 meV (450 cm^{-1}) is considered for all reactions but specific values, as in the text and Tables 1 and 2, are used for $A_{1\mathrm{A/B}}^-$ oxidation. The simulations are shown in Figure S3. In Appendix S3, simulations are shown for the “large driving force” configuration employing different values of the total reorganisation energy,

λ_{tot}, common to all electron transfer reactions considered. The simulations of forward electron transfer kinetics for different values of λ_{tot} are shown in Figures S4 and S5 and the simulated recombination reactions in Figure S6. In Appendix S4 are shown the simulations for specific alterations of the electron transfer parameters within the "large driving force" energetic scheme. Simulations are performed considering specific values for $\lambda_{tot,F_X \to F_A}$ and $\lambda_{tot,F_A \to F_B}$ corresponding to those employed for the "weak driving force" scenario as well as for different energetics, being exactly the same as those reported in ref. [24] but with the remaining parameter as in the main text and Table 2. The simulated forward electron transfer reactions are shown in Figure S7 and the recombination in Figure S8.

Author Contributions: "Conceptualization, software, writing—original draft: S.S.; methodology, investigation, preparation, writing—review and editing S.S & A.P.C. All authors have read and agreed to the published version of the manuscript."

Funding: This study was economically supported by Regione Lombardia through the project "Enhancing Photosynthesis" (DSS 16652 30/11/2021) on behalf of the winners of the "Lombardia è Ricerca – 2020" award and by MUR through the National Recovery and Resilience Plan (NRRP/PNRR), Mission 4, Component C2, Investment 1.1, Call for tender No. 104 of the 02/02/202 2 by the Italian Ministry of University and Research (MUR), funded by the European Union –NextGenerationEU– Project Title "Extending the red limit of oxygenic photosynthesis: basic principles and implications for future applications (20224HJWMH)" – CUPs B53D23015880006 Grant Assignment Decree No. 1017 adopted on 07/07/2023 by MUR.

Data Availability Statement: Dataset available on request from the authors

Conflicts of Interest: The authors declare no conflicts of interest.

References

1. Caffarri S, Tibiletti T, Jennings RC, Santabarbara S (2014) A comparison between plant photosystem I and photosystem II architecture and functioning. *Curr Protein Pept Sci* 15, 296-331
2. Srinivasan, N., Golbeck, J.H. (2009) Protein-cofactor interactions in bioenergetic complexes: The role of the A_{1A} and A_{1B} phylloquinones in Photosystem I. *Biochim Biophys Acta* 1787, 1057-1088
3. Jordan P, Fromme P, Witt HT, Klukas O, Saenger W, Krauss N (2001) Three-dimensional structure of cyanobacterial photosystem I at 2.5 angstrom resolution. Nature 411: 909-917
4. Mazor, Y., Borovikova, A., Caspy, I., Nelson, N. (2017) Structure of the plant photosystem I supercomplex at 2.6 Å resolution. *Nat. Plants* 3:17014. doi: 10.1038/nplants.2017
5. Qin, X., Suga, M., Kuang, T., Shen, J.R. (2015) Photosynthesis. Structural basis for energy transfer pathways in the plant PSI-LHCI supercomplex. *Science* 348, 989–995. doi: 10.1126/science.aab0214
6. Brettel, K. (1997) Electron transfer and arrangement of the redox cofactors in photosystem I. *Biochim. Biophys. Acta* 1318, 322–373. doi: 10.1016/S0005-2728(96)00112-0
7. Santabarbara, S., Heathcote, P., Evans, M.C.W. (2005) Modelling of the electron transfer reactions in Photosystem I by electron tunnelling theory. *Biochim. Biophys. Acta* 1708, 283–310. doi: 10.1016/j.bbabio.2005.05.001
8. Rappaport, F., Diner, B.A., Redding, K.E. (2006) "Optical Measurements of Secondary Electron Transfer in Photosystem I," in *Photosystem I: The Light–Driven Plastocyanin:Ferredoxin Oxidoreductase*, ed. J.H. Golbeck (Dordrecht, Kluwer Academic Publishers), 223–244. doi: 10.1007/978-1-4020-4256-0_16
9. Redding, K.E., van der Est, A. (2006). "The Directionality of Electron Transport in Photosystem I," in *Photosystem I: The Light–Driven Plastocyanin:Ferredoxin Oxidoreductase*, ed. J.H. Golbeck (Dordrecht, Kluwer Academic Publishers), 413–437. doi: 10.1007/978-1-4020-4256-0_25
10. Santabarbara, S., Galuppini, L., Casazza, A.P. (2010). Bidirectional electron transfer in the reaction centre of photosystem I. *J. Integr. Plant. Biol.* 52, 735–749. doi: 10.1111/j.1744-7909.2010.00977.x
11. Makita, H., Hastings, G. (2016) Modeling electron transfer in photosystem I. *Biochim. Biophys. Acta* 1857, 723–733. doi: 10.1016/j.bbabio.2016.03.015
12. Santabarbara S., Casazza A.P., Hastings G. (2019) Modelling electron transfer in photosystem I: limits and perspectives. *Physiol. Plant.* 166, 73–87
13. Santabarbara, S., Kuprov, I., Fairclough, W.V., Purton, S., Hore, P.J., Heathcote, P., Evans, M.C.W. (2005) Bidirectional electron transfer in photosystem I: determination of two distances between P_{700}^{+} and A_1^{-} in spin-correlated radical pairs. *Biochemistry* 44, 2119–2128. doi: 10.1021/bi048445d
14. Poluektov, O.G., Paschenko, S.V., Utschig, L.M., Lakshmi, K.V., Thurnauer, M.C. (2005) Bidirectional electron transfer in photosystem I: direct evidence from high-frequency time-resolved EPR spectroscopy. *J. Am. Chem. Soc.* 127, 11910–11911. doi: 10.1021/ja053315t

15. Santabarbara, S., Kuprov, I., Hore, P.J., Casal, A., Heathcote, P., Evans, M.C.W. (2006) Analysis of the spin-polarized electron spin echo of the $[P_{700}^{+}A_1^{-}]$ radical pair of photosystem I indicates that both reaction center subunits are competent in electron transfer in cyanobacteria, green algae, and higher plants. *Biochemistry* 45, 7389–7403. doi: 10.1021/bi060330h
16. Ramesh, V.M., Gibasiewicz, K., Lin, S., Bingham, S.E., A Webber, A.N. (2007) Replacement of the methionine axial ligand to the primary electron acceptor A_0 slows the A_0^{-} reoxidation dynamics in Photosystem I. *Biochim. Biophys. Acta* 1767, 151–160
17. Giera, W., Gibasiewicz, K., Ramesh, V.M., Lin, S., Webber, A. (2009) Electron transfer from A_0^{-} to A_1 in Photosystem I from *Chlamydomonas reinhardtii* occurs in both the A and B branch with 25-30-ps lifetime. *Phys. Chem. Chem. Phys.* 11, 5186–5191
18. Santabarbara, S., Kuprov, I., Poluektov, O.G., Casal, A., Russell, C.A., Purton, S., Evans, M.C.W. (2010) Directionality of electron-transfer reactions in photosystem I of prokaryotes: universality of the bidirectional electron-transfer model. *J. Phys. Chem. B* 114, 15158–15171. doi: 10.1021/jp1044018
19. Poluektov, O.G, Utschig, L.M. (2015) Directionality of Electron Transfer in Type I Reaction Center Proteins: High-Frequency EPR Study of PS I with Removed Iron−Sulfur Centers. *J. Phys. Chem. B* 119, 13771−13776
20. Xu, W., Chitnis, P.R., Valeva, A., van der Est, A., Brettel, K., Guergova-Kuras, M. et al. (2003) Electron transfer in cyanobacterial photosystem I: II. Determination of forward electron transfer rates of site-directed mutants in a putative electron transfer pathway from A_0 through A_1 to F_X. *J. Biol. Chem.* 278, 27876–27887. doi: 10.1074/jbc.M302965200
21. Cohen, R.O., Shen, G., Golbeck, J.H., Xu, W., Chitnis, P.R., Valieva, A.I., van der Est, A., Pushkar, Y., Stehlik, D. (2004) Evidence for asymmetric electron transfer in cyanobacterial photosystem I: analysis of a methionine-to-leucine mutation of the ligand to the primary electron acceptor A_0. *Biochemistry* 43, 4741–4754. doi: 10.1021/bi035633f
22. Dashdorj, N., Xu, W., Cohen, R.O., Golbeck, J.H., Savikhin, S. (2005) Asymmetric electron transfer in cyanobacterial Photosystem I: charge separation and secondary electron transfer dynamics of mutations near the primary electron acceptor A_0. *Biophys. J.* 88, 1238–12349. doi: 10.1529/biophysj.104.050963
23. Sun, J., Hao, S., Radle, M., Xu, W., Shelaev, I., Nadtochenko, V., Shuvalov, V., Semenov, A.Yu., Gordon, H., van der Est, A., Golbeck, J.H. (2014) Evidence that histidine forms a coordination bond to the A_{0A} and A_{0B} chlorophylls and a second H-bond to the A_{1A} and A_{1B} phylloquinones in $M688H_{PsaA}$ and $M668H_{PsaB}$ variants of *Synechocystis sp.* PCC 6803. *Biochim. Biophys. Acta*. 1837, 1362–1375. doi: 10.1016/j.bbabio.2014.04.004
24. Milanovsky, G.E., Ptushenko, V.V., Golbeck, J.H., Semenov, A.Y., Cherepanov, D.A. (2014) Molecular dynamics study of the primary charge separation reactions in Photosystem I: effect of the replacement of the axial ligands to the electron acceptor A_0. *Biochim. Biophys. Acta* 1837, 1472–1483. doi: 10.1016/j.bbabio.2014.03.001
25. Joliot, P., Joliot, A. (1999) In vivo analysis of the electron transfer within photosystem I: are the two phylloquinones involved? *Biochemistry* 38, 11130–11136. doi: 10.1021/bi990857c
26. Brettel, K., Leibl, W. (2001) Electron transfer in photosystem I. Biochim Biophys Acta 1507, 100-114
27. Guergova-Kuras, M., Boudreaux, B., Joliot, A., Joliot, P., Redding, K.E. (2001) Evidence for two active branches for electron transfer in photosystem I. *Proc. Natl. Acad. Sci. U.S.A.* 98, 4437–4442. doi: 10.1073/pnas.081078898
28. Fairclough, W.V, Forsyth, A., Evans, M.C.W., Rigby, S.E.J., Purton, S. Heathcote, P. (2003) Bidirectional electron transfer in photosystem I: electron transfer on the PsaA side is not essential for phototrophic growth in Chlamydomonas. *Biochim Biophys. Acta* 1606, 43–55
29. Purton, S., Stevens, D.R., Muhiuddin, I.P., Evans, M.C., Carter, S., Rigby, S.E., Heathcote, P. (2001). Site-directed mutagenesis of PsaA residue W693 affects phylloquinone binding and function in the photosystem I reaction center of *Chlamydomonas reinhardtii*. Biochemistry 40, 2167–2175. doi: 10.1021/bi0019489
30. Byrdin, M., Santabarbara, S., Gu, F., Fairclough, V.W., Heathcote, P., Redding, K.E., Rappaport, F. (2006) Assignment of a kinetic component to electron transfer between iron-sulfur clusters F_X and $F_{A/B}$ of Photosystem I. *Biochim. Biophys. Acta* 1757, 1529–1538. doi: 10.1016/j.bbabio.2006.06.016
31. Ali, K., Santabarbara, S., Heathcote, P., Evans, M.C.W., Purton, S. (2006) Bidirectional electron transfer in photosystem I: replacement of the symmetry-breaking tryptophan close to the PsaB-bound phylloquinone A_{1B} with a glycine residue alters the redox properties of A_{1B} and blocks forward electron transfer at cryogenic temperatures. *Biochim. Biophys. Acta* 1757, 1623–1633. doi: 10.1016/j.bbabio.2006.07.006
32. Schlodder, E., Falkenberg, K., Gergeleit, M., Brettel, K. (1998). Temperature dependence of forward and reverse electron transfer from A_1^{-}, the reduced secondary electron acceptor in photosystem I. *Biochemistry* 37, 9466–9476. doi: 10.1021/bi973182r
33. Agalarov, R., and Brettel, K. (2003). Temperature dependence of biphasic forward electron transfer from the phylloquinone(s) A_1 in photosystem I: only the slower phase is activated. *Biochim. Biophys. Acta* 1604, 7–12. doi: 10.1016/S0005-2728(03)00024-0

34. Santabarbara, S., Redding, K.E., Rappaport, F. (2009). Temperature dependence of the reduction of P_{700}^{+} by tightly bound plastocyanin *in vivo*. *Biochemistry* 48, 10457–10466. doi: 10.1021/bi901052c
35. Marcus, R.A., and Sutin, N. (1985). Electron transfer in chemistry and biology. *Biochim. Biophys. Acta* 811, 265–322. doi: 10.1016/0304-4173(85)90014-X
36. Devault, D. (1980). Quantum mechanical tunnelling in biological systems. Cambridge University Press
37. Moser, C.C., and Dutton, P.L. (1992). Engineering protein structure for electron transfer function in photosynthetic reaction centers. *Biochim. Biophys. Acta* 1101, 171–176. doi: 10.1016/0005-2728(92)90205-G
38. Moser, C.C., and Dutton, P.L. (2006). "Application of Marcus Theory to Photosystem I Electron Transfer," in *Photosystem I: The Light–Driven Plastocyanin:Ferredoxin Oxidoreductase*, ed. J.H. Golbeck (Dordrecht, Kluwer Academic Publishers), 583–594
39. Milanovsky, G.E., Petrova, A.A., Cherepanov, D.A, Semenov A.Yu. (2017) Kinetic modeling of electron transfer reactions in photosystem I complexes of various structures with substituted quinone acceptors. *Photosynth. Res.* 133, 185–199. doi: 10.1007/s11120-017-0366-y
40. Munge, B., Das, S.K., Ilagan, R., Pendon, Z., Yang, J., Frank, H.A., Rusling, J.F. (2003) Electron transfer reactions of redox cofactors in spinach Photosystem I reaction centre proteins in lipid films on electrodes. *J. Am. Chem. Soc.* 125, 12457–12463. doi: 10.1021/ja036671p
41. Ke, B., Dolan, E., Sugahara, K., Hawkridge, F.M., Demeter, S., Shaw E. (1977) Electrochemical and kinetic evidence for a transient electron transfer acceptor in the photochemical charge separation in photosystem I. *Plant Cell Physiol.* 3-7, 187–199
42. Chamorowsky, S.K., and Cammack, R. (1982) Direct determination of the midpoint potential of the acceptor X in chloroplast Photosystem I by electrochemical reduction and electron spin resonance. *Photochem. Photobiophys.* 4, 195–200
43. Parrett, K.G., Mehari, T., Warren, P.G., Golbeck, J.H. (1989) Purification and properties of the intact P700- and Fx-containing Photosystem I core protein. *Biochim. Biophys. Acta* 973, 324–332. doi:10.1016/S0005-2728(89)80439-6
44. Ptushenko, V.V., Cherepanov, D.A., Krishtalik, L.I., Semenov, A.Y. (2008). Semi-continuum electrostatic calculations of redox potentials in photosystem I. *Photosynth. Res.* 97, 55–74. doi: 10.1007/s11120-008-9309-y
45. Ishikita, H., Knapp, E.W. (2003) Redox potential of quinones in both electron transfer branches of photosystem I. *J Biol Chem* 278, 52002-52011
46. Karyagina, I., Pushkar, Y., Stehlik, D., van der Est, A., Ishikita, H., Knapp, E,W,, Jagannathan, B., Agalarov, R., Golbeck, J.H. (2007) Contributions of the protein environment to the midpoint potentials of the A_1 phylloquinones and the Fx iron-sulfur cluster in photosystem I. *Biochemistry* 46, 10804-10816
47. Kawashima, K., Ishikita, H. (2017) Structural Factors That Alter the Redox Potential of Quinones in Cyanobacterial and Plant Photosystem I. *Biochemistry* 56, 3019-3028
48. Santabarbara, S., Zucchelli, G. (2016) Comparative kinetic and energetic modelling of phyllosemiquinone oxidation in Photosystem I. *Phys. Chem. Chem. Phys.* 18, 9687–9701. doi: 10.1039/C5CP06590A
49. Santabarbara, S. Casazza, A.P. (2019) Kinetics and Energetics of Phylloquinone Reduction in Photosystem I: Insight From Modeling of the Site Directed Mutants. *Front. Plant Sci.* 10, 852. doi: 10.3389/fpls.2019.00852
50. Ke, B., Hansen, R.E., Beinert, H. (1973) Oxidation-reduction potentials of bound iron-sulfur proteins of photosystem I. *Proc. Natl. Acad. Sci. U.S.A.* 70, 2941–2945. doi: 10.1073/pnas.70.10.2941
51. Evans, M.C.W., Reeves, S.G, Cammack, R. (1974) Determination of the oxidation-reduction potential of the bound iron–sulphur proteins of the primary electron acceptor complex of Photosystem I in spinach chloroplasts. *FEBS Lett.* 49, 111–114. doi:10.1016/0014-5793(74)80644-7
52. Evans, M.C.W., and Heathcote, P. (1980) Effects of glycerol on the redox properties of the electron acceptor complex in spinach photosystem I particles. *Biochim Biophys Acta* 590: 89–96. doi.org/10.1016/0005-2728(80)90148-6
53. Nugent, J.H., Moller, B.L., Evans, M.C.W. (1981) Comparison of the EPR properties of Photosystem I iron–sulphur centres A and B in spinach and barley. *Biochim. Biophys. Acta* 634, 249–255. doi.org/10.1016/0005-2728(81)90143-2
54. Hiyama, T., Ke, B. (1971) A further study of P430: a possible primary electron acceptor of photosystem I. *Arch. Biochem. Biophys.* 147, 99–108
55. Lüneberg, J., Fromme, P., Jekow, P., Schlodder, E. (1994) Spectroscopic characterization of PS I core complexes from thermophilic *Synechococcus sp.* Identical reoxidation kinetics of A_1^- before and after removal of the iron–sulfur-clusters F_A and F_B. *FEBS Lett.* 338, 197–202
56. Leibl, W., Toupance, B., Breton, J. (1995) Photoelectric characterization of forward electron transfer to iron–sulfur centers in photosystem I. *Biochemistry* 34, 10237–10244

57. Diaz-Quintana, A., Leibl, W., Bottin, H., Setif, P. (1998) Electron transfer in photosystem I reaction centers follows a linear pathway in which iron-sulfur cluster F_B is the immediate electron donor to soluble ferredoxin. *Biochemistry* 37, 3429–3439
58. Mamedov, M.D., Gourovskaya, K.N., Vassiliev, I.R., Golbeck ,J.H., Semenov, A.Yu. (1998) Electrogenicity accompanies photoreduction of the iron-sulfur clusters F_A and F_B in photosystem I. *FEBS Lett.* 431, 219–223
59. Mamedova, A.A., Mamedov, M.D., Gourovskaya, K.N., Vassiliev, I.R., Golbeck, J.H., Semenov, A.Yu. (1999) Electrometrical study of electron transfer from the terminal F_A/F_B iron-sulfur clusters to external acceptors in photosystem I. *FEBS Lett.* 462, 421–424
60. Semenov, A.Yu., Mamedov, M.D., Chamorovsky, S.K. (2003) Photoelectric studies of the transmembrane charge transfer reactions in photosystem I pigment-protein complexes. *FEBS Lett.* 553, 223–228
61. Semenov, A.Y, Mamedov, M.D., Chamorovsky, S.K. (2006) "Electrogenic Reactions Associated with Electron Transfer in Photosystem I," in *Photosystem I: The Light–Driven Plastocyanin:Ferredoxin Oxidoreductase*, ed. J.H. Golbeck (Dordrecht, Kluwer Academic Publishers), 319–338. doi: 10.1007/978-1-4020-4256-0_16
62. Santabarbara, S., Jasaitis, A., Byrdin, M., Gu, F., Rappaport, F., Redding, K.E. (2008) Additive effect of mutations affecting the rate of phylloquinone reoxidation and directionality of electron transfer within photosystem I. *Photochem. Photobiol.* 84, 1381–1387. doi: 10.1111/j.1751-1097.2008.00458.x
63. Santabarbara, S., Bullock, B., Rappaport, F., Redding, K.E. (2015). Controlling electron transfer between the two cofactor chains of photosystem I by the redox state of one of their components. *Biophys. J.* 108, 1537–1547. doi: 10.1016/j.bpj.2015.01.009
64. Setif, P. (2001) Ferredoxin and flavodoxin reduction by photosystem I. *Biochim. Biophys. Acta* 1507, 161–179. doi: 10.1016/S0005-2728(01)00205-5
65. Hopfield, J.J. (1974). Electron transfer between biological molecules by thermally activated tunnelling. *Proc. Natl. Acad. Sci. U.S.A.* 71, 3640–3644. doi: 10.1073/pnas.71.9.3640
66. Mula, S., McConnell, M.D., Ching, A., Zhao, N., Gordon, H.L., Hastings, G., et al. (2012) Introduction of a hydrogen bond between phylloquinone PhQ_A and a threonine side-chain OH group in photosystem I. *J. Phys. Chem. B* 116, 14008–14016. doi: 10.1021/jp309410w
67. Santabarbara, S., Reifschneider, K., Jasaitis, A., Gu, F., Agostini, G., Carbonera, D., et al. (2010) Interquinone electron transfer in photosystem I as evidenced by altering the hydrogen bond strength to the phylloquinone(s). *J. Phys. Chem. B* 114, 9300–9312. doi: 10.1021/jp1038656
68. Shinkarev, V.P., Zybailov, B., Vassiliev, I.R. Golbeck, J.H. (2002) Modeling of the P_{700}^+ Charge Recombination Kinetics with Phylloquinone and Plastoquinone-9 in the A_1 Site of Photosystem I. *Biophys. J.* 83, 2885–2897
69. Makita, H., Hastings, G. (2017) Inverted-region electron transfer as a mechanism for enhancing photosynthetic solar energy conversion efficiency. *Proc. Natl. Acad. Sci. U.S.A.* 114, 9267–9272. doi: 10.1073/pnas.1704855114
70. Kurashov, V., Gorka, M., Milanovsky, G.E., Johnson, T.W., Cherepanov, D.A., Semenov, A.Yu., Golbeck, J.H. (2018) Critical evaluation of electron transfer kinetics in P_{700}–F_A/F_B, P_{700}–F_X, and P_{700}–A_1 Photosystem I core complexes in liquid and in trehalose glass. *Biochim. Biophys. Acta* 1859, 1288–1301
71. Milanovsky, G., Gopta, O., Petrova, A.A, Mamedov M.D., Gorka, M., Cherepanov, D.A., Golbeck, J.H., Semenov, A.Yu. (2019) Multiple pathways of charge recombination revealed by the temperature dependence of electron transfer kinetics in cyanobacterial photosystem I. *Biochim. Biophys. Acta* 1860, 601–610
72. Cherepanov, D.A., Milanovsky, G.E., Gopta, O.A., Balasubramanian, R., Bryant, D.A., Semenov, A.Yu., Golbeck, J.H. (2018) Electron-Phonon Coupling in Cyanobacterial Photosystem I. *J. Phys. Chem. B.* 122, 7943–7955. doi: 10.1021/acs.jpcb.8b03906
73. Zhao, J., Li N., Warren, P.V., Golbeck, J.H., Bryant, D.A. (1992) Site-directed conversion of a cysteine to aspartate leads to the assembly of a [3Fe-4S] cluster in PsaC of photosystem I. The photoreduction of F_A is independent of F_B. *Biochemistry* 31, 5093-5099. doi: 10.1021/bi00137a001
74. Rodday, S.M., Jun, S.S., Biggins, J. (1993) Interaction of the F_AF_B-containing subunit with the Photosystem 1 core heterodimer. *Photosynth. Res.* 36, 1-9. doi: 10.1007/BF00018069
75. Yu, L., Zhao, .J, Lu, W., Bryant, D.A., Golbeck, J.H. (1993) Characterization of the [3Fe-4S] and [4Fe-4S] clusters in unbound PsaC mutants C14D and C51D. Midpoint potentials of the single [4Fe-4S] clusters are identical to F_A and F_B in bound PsaC of photosystem I. *Biochemistry* 32, 8251-8258. doi: 10.1021/bi00083a028
76. Yu, L., Bryant, D.A., Golbeck, J.H. (1995) Evidence for a mixed-ligand [4Fe-4S] cluster in the C14D mutant of PsaC. Altered reduction potentials and EPR spectral properties of the F_A and F_B clusters on rebinding to the P700-FX core. *Biochemistry* 34, 7861-7868. doi: 10.1021/bi00024a010
77. Mehari, T., Qiao, F., Scott, M.P., Nellis, D.F., Zhao, J., Bryant, D.A., Golbeck, J.H. (1995) Modified ligands to F_A and F_B in photosystem I. I. Structural constraints for the formation of iron-sulfur clusters in free and rebound PsaC. J. Biol. Chem. 270, 28108-28117. doi: 10.1074/jbc.270.47.28108

78. Rodday, S.M., Do, L.T., Chynwat, V., Frank, H.A., Biggins, J. (1996) Site-directed mutagenesis of the subunit PsaC establishes a surface-exposed domain interacting with the photosystem I core binding site. *Biochemistry* 35, 11832-11838. doi: 10.1021/bi9612834
79. Jung, Y..S, Vassiliev, I.R., Qiao, F., Yang, F., Bryant, D.A., Golbeck, J.H. (1996) Modified ligands to F_A and F_B in photosystem I. Proposed chemical rescue of a [4Fe-4S] cluster with an external thiolate in alanine, glycine, and serine mutants of PsaC. *J. Biol. Chem.* 271, 31135-31144. doi: 10.1074/jbc.271.49.31135
80. Yu, J., Vassiliev, I.R., Jung, Y.S., Golbeck, J.H., McIntosh, L. (1997) Strains of *synechocystis sp*. PCC 6803 with altered PsaC. I. Mutations incorporated in the cysteine ligands of the two [4Fe-4S] clusters F_A and F_B of photosystem I. *J. Biol. Chem.* 272, 8032-8039. doi: 10.1074/jbc.272.12.8032
81. Jung, Y.S., Vassiliev, I.R., Yu, J., McIntosh, L., Golbeck, J.H. (1997) Strains of *Synechocystis sp*. PCC 6803 with altered PsaC. II. EPR and optical spectroscopic properties of F_A and F_B in aspartate, serine, and alanine replacements of cysteines 14 and 51. *J. Biol. Chem.* 272, 8040-8049. doi: 10.1074/jbc.272.12.8040
82. Fischer, N., Setif, P., Rochaix, J-D. (1997) Targeted Mutations in the psaC Gene of *Chlamydomonas reinhardtii*: Preferential reduction of F_B at low temperature is not accompanied by altered electron flow from Photosystem I to Ferredoxin. *Biochemistry* 36, 93–102
83. Fischer, N., Setif, P., Rochaix, J-D. (1999) Site-directed Mutagenesis of the PsaC Subunit of Photosystem I. FB is the cluster interacting with soluble ferredoxin. *J. Biol. Chem.* 33, 23333–23340
84. Pérez, A.A., Ferlez, B.H., Applegate, A.M., Walters, K., He, Z., Shen, G., Golbeck, J.H., Bryant, D.A. (2018) Presence of a [3Fe-4S] cluster in a PsaC variant as a functional component of the photosystem I electron transfer chain in *Synechococcus sp*. PCC 7002.. *Photosynth Res*. 136, 31–48. doi: 10.1007/s11120-017-0437-0
85. Webber, A.N., Gibbs, P.B., Ward, J.B., Bingham, S.E. (1993) Site-directed mutagenesis of the photosystem I reaction center in chloroplasts. The proline-cysteine motif. *J. Biol. Chem.* 268, 12990–12995
86. Smart, L.B., Warren, P.V., Golbeck, J.H., McIntosh, L. (1993) Mutational analysis of the structure and biogenesis of the photosystem I reaction center in the cyanobacterium *Synechocystis* sp. PCC 6803. *Proc. Natl. Acad. Sci. U.S.A.* 90, 1132–1136. doi: 10.1073/pnas.90.3.1132
87. Warren, P.V., Smart, L.B., McIntosh, L., Golbeck, J.H. (1993) Site-directed conversion of cysteine-565 to serine in PsaB of photosystem I results in the assembly of [3Fe-4S] and [4Fe-4S] clusters in F_X. A mixed-ligand [4Fe-4S] cluster is capable of electron transfer to F_A and F_B. *Biochemistry* 32, 4411–4419. doi: 10.1021/bi00067a034
88. Rodday, S.M., Schulz, R., McLntosh, L., Biggins, J. (1994) Structure-function studies on the interaction of PsaC with the Photosystem 1 heterodimer : The site directed change R561E in PsaB destabilizes the subunit interaction in *Synechocystis sp*. PCC 6803. *Photosynth. Res*. 42, 185–190. doi: 10.1007/BF00018261
89. Rodday, S.M., Webber, A.N., Bingham, S.E., Biggins, J. (1995) Evidence that the FX domain in photosystem I interacts with the subunit PsaC: site-directed changes in PsaB destabilize the subunit interaction in *Chlamydomonas reinhardtii*. *Biochemistry* 34, 6328–6334. doi: 10.1021/bi00019a010
90. Hallahan, B.J., Purton, S., Ivison, A., Wright, D., Evans, M.C.W. (1995) Analysis of the proposed Fe-S_X binding region of Photosystem 1 by site directed mutation of PsaA in *Chlamydomonas reinhardtii*. *Photosynth Res*. 46, 257–264. doi: 10.1007/BF00020438
91. Vassiliev, I.R., Jung, Y-S., Smart, L.B., Schulz, R., McIntosh, L. Golbeck, J.H. (1995) A Mixed-Ligand Iron-Sulfur Cluster (C556SPSaB or C565SPSaB) in the F_X-Binding Site Leads to a Decreased Quantum Efficiency of Electron Transfer in Photosystem I. *Biophys. J.* 69, 1544–1553
92. Evans, M.C.W., Purton, S. Patel, V., Wright, D., Heathcote, P., Rigby, S.E.J. (1999) Modification of electron transfer from the quinone electron carrier, A_1, of Photosystem 1 in a site directed mutant D576->L within the Fe-Sx binding site of PsaA and in second site suppressors of the mutation in *Chlamydomonas reinhardtii*. *Photosynth. Res.* 61, 33–42
93. Vassiliev, I.R., Yu, J., Jung, Y-S., Schulz, R., Ganago, A.O., McIntosh, L., Golbeck, J.H. (1999) The Cysteine-proximal Aspartates in the F_X-binding Niche of Photosystem I. *J. Biol. Chem.* 274, 9993–10001
94. Zeng, M-T., Gong, X-M., Evans, M.C.W., Nelson, N., Carmeli, C. (2002) Stabilization of iron–sulfur cluster F_X by intra-subunit interactions unraveled by suppressor and second site-directed mutations in PsaB of Photosystem I. *Biochim. Biophys. Acta* 1556, 254– 264
95. Gong, X-M., Agalarov, R., Brettel, K., Carmeli, C. (2003) Control of Electron Transport in Photosystem I by the Iron-Sulfur Cluster F_X in Response to Intra- and Intersubunit Interactions. *J. Biol. Chem.* 278, 19141–19150. doi 10.1074/jbc.M301808200
96. Kümmerle, R., Gaillard, J. Kyritis, P., Moulis J.-M. (2001) Intramolecular electron transfer in [4Fe-4S] proteins: estimates of the reoganisation energy and electronic coupling in *Chromatium vinosum* ferredoxin *J. Biol. Inorg. Chem.* 6, 446–451